EÖTVÖS LORÁND UNIVERSITY

FACULTY OF INFORMATICS

INSTITUTE OF CARTOGRAPHY AND GEOINFORMATICS

# Multispectral satellite-based water surface mapping in Nhecolândia, Brazilian Pantanal

**Pietro Laba Cabral de Menezes**

student of Cartography MSc

**András Jung**

Associate Professor

ELTE Institute of Cartography and Geoinformatics

Budapest, 2023

# ACKNOWLEDGMENT

*"But the delight and pride is in the deed of making, and in the thing made, and neither in possession nor in his own mastery."*

J.R.R. Tolkien

# Table of Contents

# LIST OF FIGURES

# LIST OF TABLES

**ABSTRACT**

Water plays an important role in the ecosystems of the earth and even more important in the swamplands. This study builds a workflow that can be programmatically applied in Sentinel-2 datasets to monitor water surface area in the Brazilian Pantanal. Also, the state of the hydrography of the Nhecolândia region between the years of 2016 and 2022 was assessed to verify the applicability of the method. By using water extraction indexes coupled with Otsu's thresholding algorithm, the study appraised the applicability of five different indexes: normalized difference water index (NDWI), modified normalized difference water index (MNDWI), new water index (NWI), Sentinel-2 water index (SWI) and automated water extraction index for shadow areas (AWEIsh). The results show that for the target area the AWEIsh index had the best accuracy, with a kappa index of 0,87, and it was applied to the entirety of the datasets, resulting in 14 water extraction maps. From these, it was possible to observe a steady decrease in water surface area between the years of 2016 and 2022 and most importantly a sharp decrease in the year of 2020. From water surface change calculations, the peak water surface area of the region measured was 238 $km^2$ while the lowest was 4 $km^2$. The surface water area during the wet season suffered a decrease of 83% in the spam of the study and, on average, a decrease of 75% between the wet and dry season each year.

**Keywords:** Pantanal, remote sensing, surface water detection, spectral index, time-series, climate-change, Sentinel-2

# 1. INTRODUCTION

Water plays an essential role in the life of most of the living creatures in our planet. In the last few years awareness about this resource availability has been raised dramatically, mostly in the context of climate changes related to global warming (Gleick, 1993). Therefore, monitoring and assessing water reservoirs has become an even more important subject.

There is around 1386 million $km^3$ of water available on Earth, from this total only 0,0008% is available in swamplands (Shiklomanov, 1993). Even though the volume of water in swamplands compared to the total doesn't seem expressive, these reservoirs deeply affect the communities and biota located nearby them.

The Brazilian Pantanal is one of the largest wetlands of the planet and is recognized by UNESCO as a World Biosphere Reserve due to its complex and diverse natural characteristics. Due to its semi-arid nature, the area is highly vulnerable to severe floods and droughts (Marengo et al., 2016). Therefore, tools to analyze and monitor climate change impacts in the region are becoming increasingly important.

Since the 1970s and the launch of the first remote sensing satellite missions, a new tool was available for water reservoirs assessment. In the following decades, further improved sensors were launched, and more sophisticated methods are available. Nowadays, remote sensing techniques represent an easily accessible and cheaper technique than in situ measurements of water surfaces (Bijeesh-Narasimhamurthy, 2020). Due to the restricted access and human occupation of the area, the employment of remote sensing methods at the region is imperative.

This work aims to provide a workflow that allows the monitoring of the surface water at the Brazilian Pantanal. For this, the present study analyzes the viability of extracting water surfaces using water indexes in multispectral satellite images. This workflow was developed in a manner that it could be programmatically applied and an automation without human interaction could be produced from it.

Moreover, this work also seeks to assess the changes in hydrography in the Pantanal sub-region Nhecolândia, highlighting how the variances of the climate have been influencing the region in the latest years. Lastly, this project applies datasets from the Sentinel-2 satellite which represents a new open-source sensor available to the public with higher spatial, temporal and spectral resolution than others satellites more broadly used for water sensing, such as the Landsat 5 TM, in order to spread the capabilities of this sensor.

## 2. LITERATURE REVIEW AND CONCEPTUAL BACKGROUND

### 2.1. Remote Sensing

Remote sensing is the science of acquiring, processing and interpreting data from sensor systems that digitally record the interaction between electromagnetic energy and matter. The interaction between energy and matter can be observed in the form of light, heat and microwaves and allows us to assess the physical properties of the object (Sabins- Ellis, 2020).

There are two main types of remote sensing systems: passive and active. Passive systems measure reflected solar radiation, or absorbed and reemitted solar radiation. Active systems, however, emit radiation from their own energy source towards the object and detect the radiation reflected from it (Dong-Chen, 2017).

When electromagnetic energy interacts with matter its properties can change, such as intensity, direction, wavelength, polarization and phase. The detection of these changes allows us to determine the characteristics of the matter. Five possible processes happen during these interactions (Figure 1): (a) transmission, the energy passes through the substance; (b) absorption, the energy is absorbed, mostly heating the matter; (c) emission, energy is first absorbed and then discharged; (d) scattering, the energy is deflected in all directions; (e) reflection, the energy is returned with equal angle and opposite direction to its incidence (Sabins-Ellis, 2020).
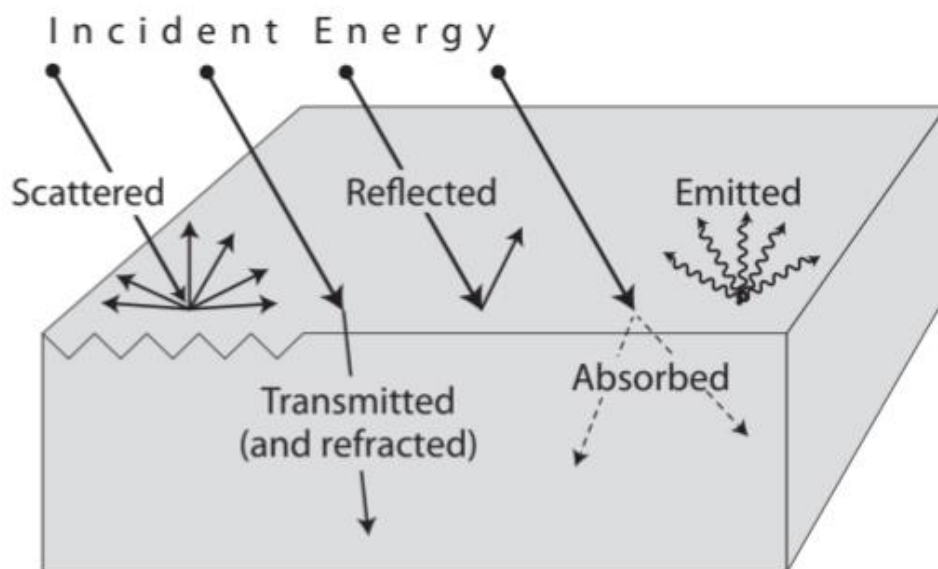


Figure 1 - Diagram showing the types of interaction between incident energy and matter and how this interaction changes the energy properties such as intensity, direction, wavelength, polarization and phase (Sabins-Ellis, 2020).

### 2.1.1. Electromagnetic Radiation

Electromagnetic radiation is the energy that moves with the speed of light ($3 \times 10^8$ ms$^{-1}$) in a harmonic wave pattern (Sabins-Ellis, 2020). This wave has the following properties (Figure 2): wavelength ($\lambda$), the distance between successive peaks; frequency ($v$), the number of times a cycle is repeated during a second; velocity (c), the speed at which the waves propagate at a certain direction, in this case the speed of light (Campbell-Wynne, 2011). These properties can be denoted by the following mathematical relation (Equation 1):

$$c = v\lambda \tag{1}$$
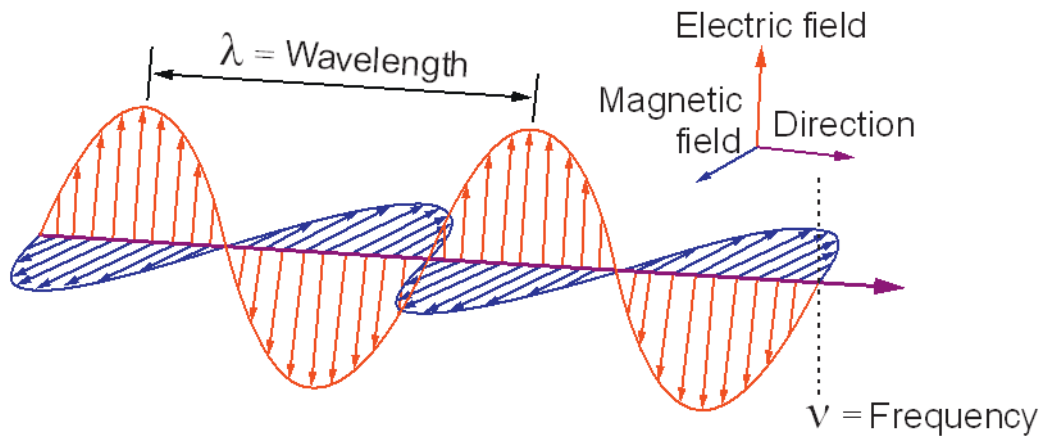


Figure 2 - Diagram with the components of an electromagnetic wave. Modified from Campbell-Wynne, 2011.

### 2.1.2. Electromagnetic Spectrum

The electromagnetic spectrum is the continuum of energy that ranges from nanometers to meters in wavelength. All matter radiates a range of electromagnetic energy that occupies a specific range of wavelength (Sabins, 2007). This spectrum is divided in different regions according to the size of the wavelength (Figure 3; Table 1).

The interaction of electromagnetic radiation with the Earth's surface generates signals known as spectral signatures. The basis of remote sensing relies in the detection of these signatures and the identification of patterns related to objects that are being analyzed (Reddy-Singh, 2018).
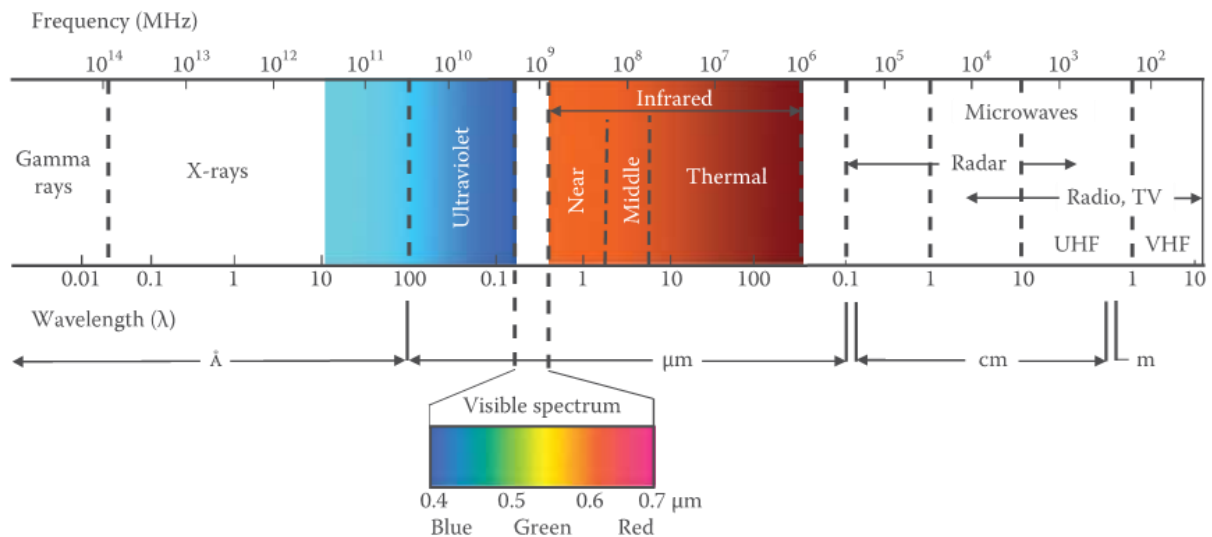
Figure 3 - Spectral bands in the electromagnetic spectrum and their respective wavelengths (Chuvieco, 2016).

Table 1 - Electromagnetic regions and bands, their wavelength and applications in the remote sensing (Chuvieco, 2016; Reddy-Singh, 2018; Sabins-Ellis, 2020).

| Spectral Region | Wavelength | Application |
|---|---|---|
| Band | | |
| Visible region | 0.4-0.7 µm | Visible spectral region where it can be detected by the human eye |
| Blue band | 0.4 - 0.5 µm | Land use, vegetation characteristics |
| Green band | 0.5 - 0.6 µm | Healthy vegetation analysis |
| Red band | 0.6 - 0.7 µm | Vegetation discrimination |
| Infrared region | 0.7 - 1000 µm | Spectral region that exceeds the human eye sensitivity range |
| Near infrared band (NIR) | 0.7 - 0.9 µm | Biomass, delineation of water features |
| Shortwave infrared (SWIR) | 0.9 - 3.0 µm | Vegetation moisture, geological materials |
| Thermal Infrared (TIR) | 3.0 - 5.0 µm | Detection of hot targets |
| Thermal Infrared (TIR) | 8.0 - 14.0 µm | Detection of warm targets, land surface temperatures |
| Microwave region | 0.1 - 100 cm | Very large wavelengths capable of penetrating through clouds and forest canopies |

## 2.1.3. Satellite Imagery

Remote sensing sensors can be mounted in a wide variety of platforms, such as cars, airplanes and backpacks. The use of satellites as remote sensing platforms, however, changed dramatically how remote sensing data could be used. Due to the orbital behavior of the satellite flight large areas could be detected with a fixed span of revisiting time, allowing for regional and temporal analysis. Another problem is related to the positioning of the satellites outside Earth's atmosphere, part of the electromagnetic radiation is scattered by the atmosphere and is detected by the satellite directly (Chuvieco, 2016). This scattered energy adds up with the target response to the electromagnetic radiation and is considered to be the total radiance (Figure 4). To acquire the actual reflectance of the targeted object, the radiance must be corrected atmospherically and remove the radiance component from sensed data (Sabins-Ellis, 2020).
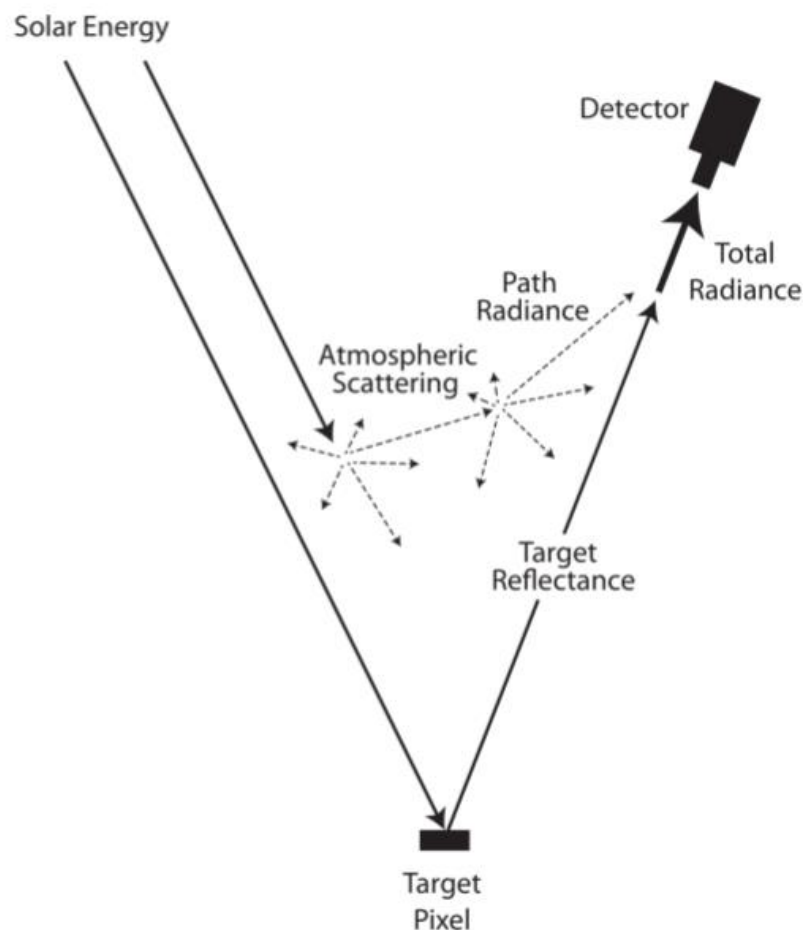


Figure 4 - Diagram representing how the atmospheric scattering sums its signal to the target reflectance resulting in the total radiance (Sabins-Ellis, 2020).

## 2.2. Remote sensing for water bodies detection

Water bodies significantly influence a region and have an irreplaceable role in global ecology and climate systems. Therefore, the monitoring of water bodies has gained increased importance in the latest years as a tool to analyze hydrological systems of a region. Contrary to in situ methods that usually are slow and resource intensive, remote sensing represents a cheap, macrographic and dynamic tool (Bijeesh, 2020).

For the effective use of remote sensing in water reservoirs analysis, the extraction and identification of water bodies is an essential step. Extensive research has been performed on this subject and four mainly used techniques can be highlighted (Yang-Chen, 2017): object-based image analysis (Castilla, 2003); pixel-based pattern recognition, supervised and unsupervised classification (Zhang et al., 2007); subpixel mapping with spectral mixture analysis (Xie et al., 2016); water indexes that enhances the water spectral difference (Mcfeeters, 1996; Xu, 2006; Feyisa, 2014).

Among these methods, water indexes have been widely used to extract water bodies, even in combination with other methods. One of the advantages of this method is the possibility to programmatically perform it, without the need of human interaction, which allows building a system to automatically extract the waterbodies from a series of images. Although this method is not flawless, each region benefits better from a specific index and their accuracy may fall dramatically in certain environments (Bijeesh, 2020).

### 2.2.1. Optical properties of the water

Water remote sensing is based on the properties highlighted by the interaction between electromagnetic radiation and water bodies. When entering a water medium, energy will undergo scattering and absorption interactions, although part of this energy will be reflected. The spectral response of the reflected energy from the water body surface is the main target of water remote sensing (Bukata, 2018).

Water has a very distinct spectral signature in the electromagnetic spectrum, most of its reflectance is in the visible wavelength (Figure 5). Therefore, the infrared and near-infrared bands can be really useful for the identification and delineation of water bodies. It is even possible to determine the nature of the water body such as pure water and turbid water using its spectral signature (Bijeesh, 2020).
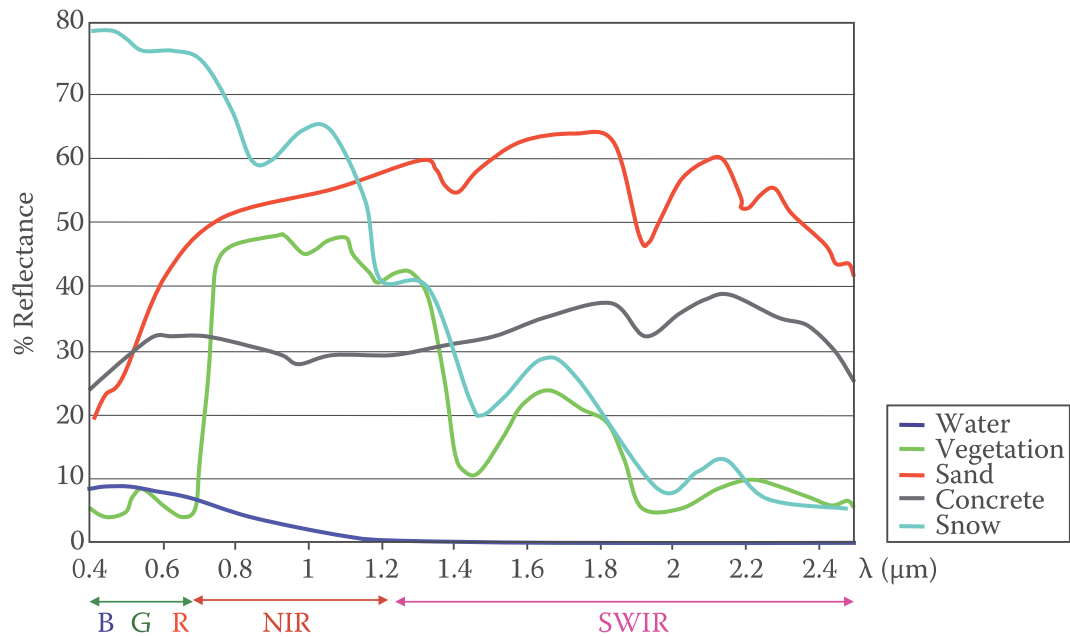
Figure 5 - Spectral reflectance signature for some of the most common materials observed in remote sensing. Modified from Chuvieco, 2016.

### 2.2.2. Satellites/sensors

Since the beginning of satellite missions at the 1970s, research of their use for water bodies detection have developed and with it the range of different sensors available. Nowadays there is a substantial range of open-source sensors capable of providing useful data for water analysis. Due to the water optical properties, any sensor capable of detecting the near-infrared region of the spectrum can be useful for water assessment, because one can easily apply a slice or threshold to the pixel values of the image to delineate water bodies (Bijeesh, 2020).

Most of the multi-spectral and hyperspectral imaging sensors available are capable of detecting the near-infrared region of the spectrum. Therefore, there is a huge library of data available for water studies. These satellites, however, have different spatial, temporal, spectral and radiometric resolutions, which restricts or enables different types of study (Guo et al., 2017). With the availability of data in higher spatial and temporal resolution in the recent years, new possibilities for detailed temporal analysis have arisen.

### 2.2.3. Sentinel-2

Sentinel-2 is a wide-swath, high-resolution, multi-spectral imaging mission launched by the Copernicus Programme under the European Space Agency (ESA). It is comprised by a constellation of two satellites, Sentinel-2A launched in 2015 and Sentinel-2B launched in 2017.

These satellites fly in the same orbit but are phased from each other by 180º, therefore the mission has a high temporal resolution of 5 days revisit frequency (Phiri et al., 2020).

The multi-spectral sensor coupled to the Sentinel-2 satellites are capable of distinguishing 13 spectral bands: four bands at 10 meters resolution, six at 20 meters resolution and three bands at 60 meters resolution. Due to the open-source nature of the mission, its data can be freely accessed in the Copernicus Programme website in different processed forms: bottom of atmosphere, already atmospheric and geometrically corrected; and top of atmosphere, which still need to undergo through correction processes before they represent the true reflectance of the sensed target (Phiri et al., 2020).

## 3. METHODOLOGY

The methodology was divided in five stages. The first stage was the literature review of the remote sensing field and its applications for water surface delineation, mainly inland water reservoirs and the application of indexes for their identification. The second step was the definition of an area of study and objective. This was followed by the acquisition and preprocessing of the images. Then, the analysis of different indexes was performed for the study area, followed by accuracy evaluation for each of them. A series of thematic maps were produced and analyzed to assess the hydrography of the study area and a water surface change tool was applied to measure the variations of the data between the years and seasons.

### 3.1. Study area

Recognized by UNESCO as a World Biosphere Reserve, the Pantanal covers approximately 140.000 $km^2$ of alluvial depression and is located in the upstream basin of the Paraguay River, stretching from the Mato Grosso state in Brazil to northern Paraguay and eastern Bolivia (Figure 6). It is characterized by a large littoral zone with a myriad of shallow lakes, which are connected through a network of channels surrounded by patches of dry land (Junk et al., 2014).

The region is a seasonally flooded alluvial plain fed by the Paraguay river and its tributaries. The flooding is heavily influenced by the precipitation pattern of the region and is marked by the rotation of two clearly defined season: a wet, from October to April; and a dry, from May to September. The hydrological cycle is divided in four different stages: rising (October to December), high water (January to March), decreasing (April to June) and low water (July to September) (da Silva-Silva, 1995).

Due to the nature of this land and its poor access, there was historically a restricted human occupation and interference. This allied to a strong interaction between abiotic and biotic elements has resulted in a great diversity of landscapes and biosphere (Bazzo et al., 2012). Besides its importance, this system is currently threatened by a wide range of human activities and its consequences. In the last years the dry season has become increasingly more severe (Figure 7) with lesser days with rain throughout the year (Lázaro et al., 2020) and it is expected a decrease of up to 30% in the rainfall by the end of the century (Marengo et al., 2016).
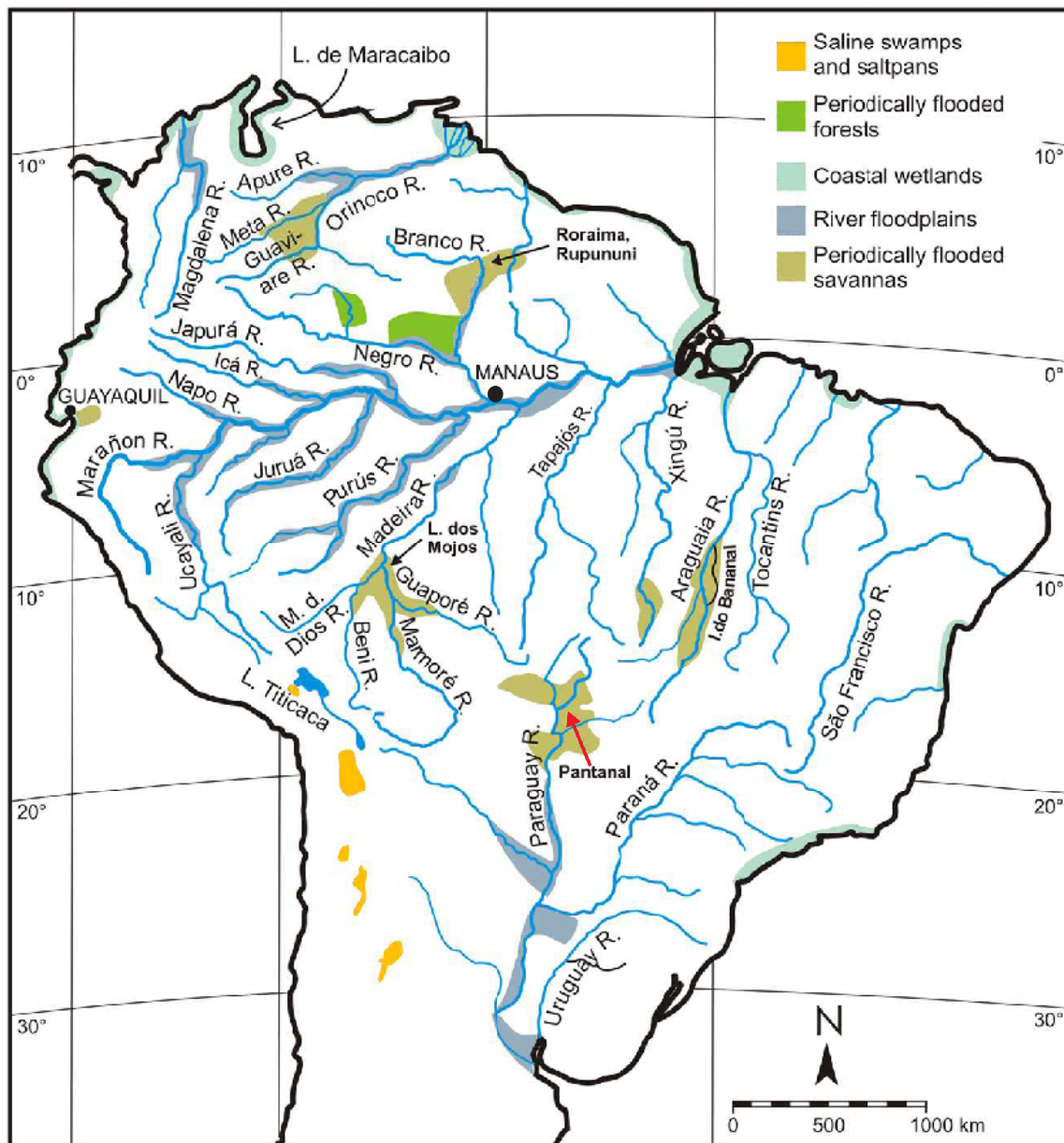
Figure 6 - Distribution of major wetlands in South America, highlighted by a red arrow the region of Pantanal. Modified from Junk et al., 2014.

The Nhecolândia sub-region is a 26.000 km$^2$ area (Figure 8), that comprises roughly 20% of the Pantanal, and is delimited at the north by the Taquari River, at the south by the Negro River, at the east by the Alegria Mountain Range and at the west by the Paraguay River (da Silva-Abdon, 1998). It has a special research importance because it is characterized as a mosaic of salt water lakes, fresh water lakes and vegetation corridors between them (Bazzo et al., 2011). To reduce computational time, a characteristic portion of the Nhecolândia sub-region with approximately 724 km$^2$ was selected (Figure 8) where the following features could be

distinguished and therefore analyzed by this work: intermittent bodies of water, permanent bodies of water, vegetation and bare soil.
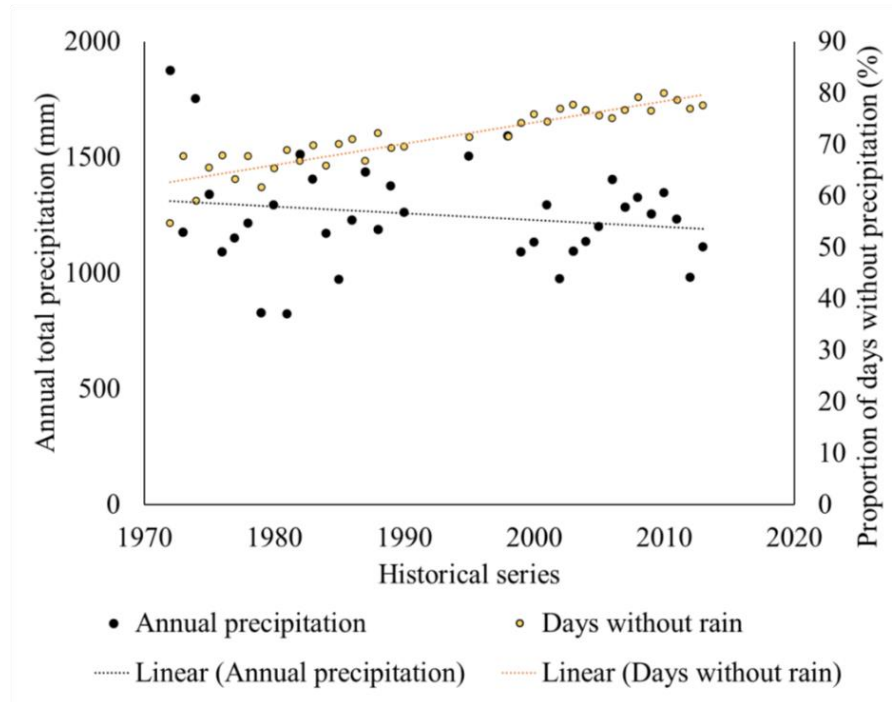


Figure 7 - Historical series of precipitation data from Pantanal from 1971 to 2013 (Lázaro et al., 2020). Showing the total precipitation per year (black dots) and the proportion of days without precipitation (yellow dots).

### 3.2. Data acquisition and preprocessing

In this project, images from Sentinel-2 were used due to its open access nature, its high spatial resolution, temporal resolution and its multispectral capacity, detecting different ranges of the infrared band that will be useful for the index calculations. The data was downloaded from the official Copernicus Program website, more specifically from the Copernicus Open Access Hub (https://scihub.copernicus.eu).

Images from the dry season and wet season from the year 2016 up until the year 2022 were downloaded. To avoid high cloud coverage, a low cloud coverage image from the whole period of the high water stage and one of the whole period of the low water stage was selected for each year, as close as possible to the end of the stage (Table 2).

The Sentinel-2 files downloaded had two distinct processing levels (Table 2): MSI – Level 1C, which is a level of preprocessing that provides an image with corrected geometry but still have Top-Of-Atmosphere (TOA) reflectance; MSI – Level 2A, which is a level of

preprocessing that already has the geometry correction and the atmospheric correction, providing a Bottom-Of-Atmosphere (BOA) reflectance. At this step the software Sen2Cor provided by the ESA was used to preprocess the images at level 1C, they received atmospheric, terrain and cirrus corrections provided by the Atmospheric Precorrected Differential Absorption algorithm (Louis et al., 2016) and the resulting data is a level 2A image with BOA reflectance (Pignatale, 2022). Finally, the entirety of the dataset was clipped to the extent of the study target area using the software QGIS 3.22.
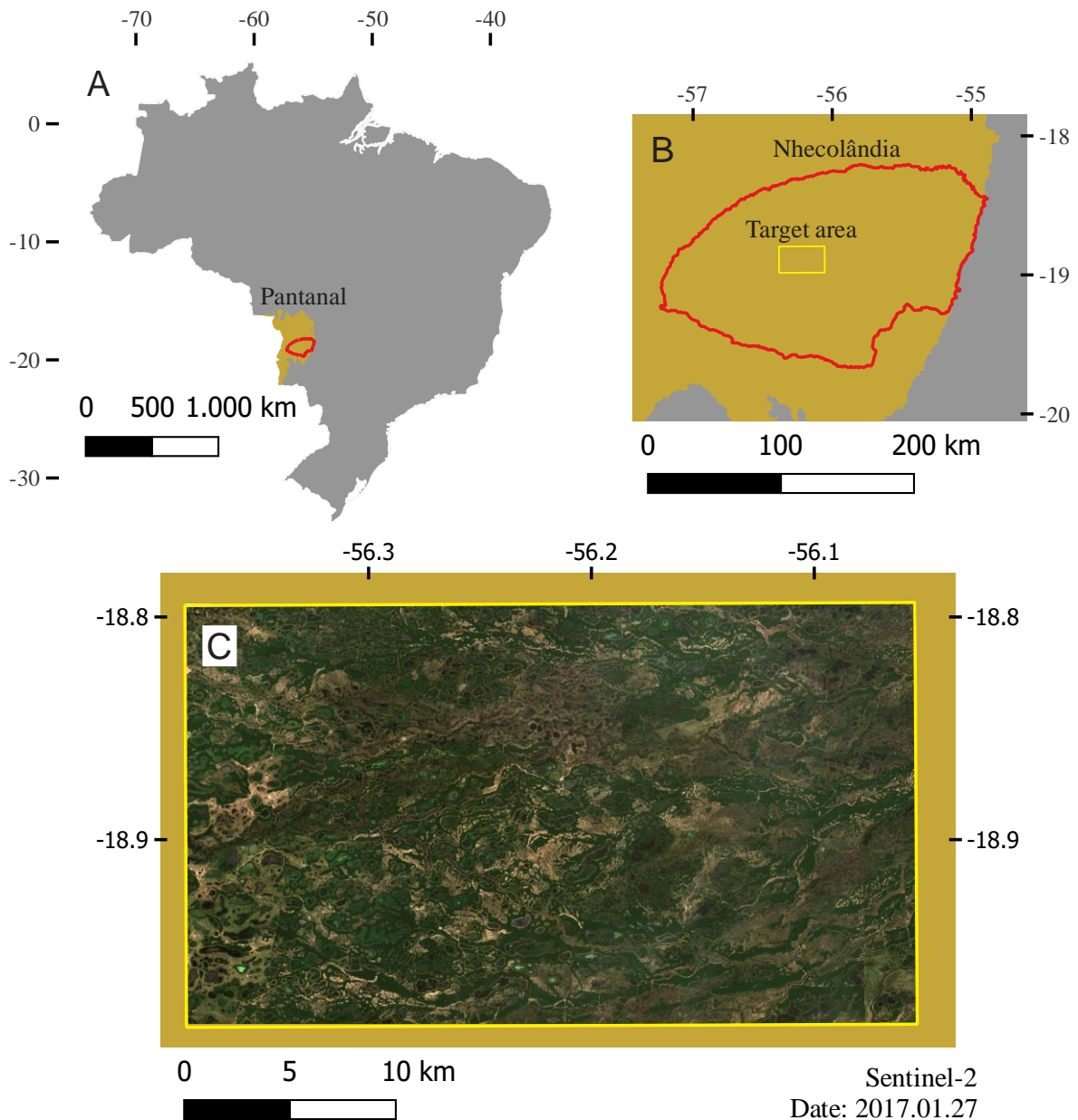


Figure 8 - A) Location of the Pantanal inside Brazil, in red the Nhecolândia sub-region. B) Location of the target area in the Nhecolândia context. C) True color image from the Sentinel-2 sensor sensed during the high water stage in 2017.01.27.

Table 2 - Acquisition date, processing level and stage of the satellite imagery downloaded from the Copernicus Open Acess Hub.

| Acquisition Date | Processing Level | Stage |
|:---:|:---:|:---:|
| 2016.03.13 | 1C | High Water |
| 2016.09.09 | 1C | Low Water |
| 2017.01.12 | 1C | High Water |
| 2017.09.19 | 1C | Low Water |
| 2018.02.06 | 1C | High Water |
| 2018.09.24 | 1C | Low Water |
| 2019.02.01 | 2A | High Water |
| 2019.09.24 | 2A | Low Water |
| 2020.03.21 | 2A | High Water |
| 2020.09.23 | 2A | Low Water |
| 2021.03.27 | 2A | High Water |
| 2021.09.28 | 2A | Low Water |
| 2022.02.25 | 2A | High Water |
| 2022.08.14 | 2A | Low Water |

*3.3. Index calculation and classification*

The delineation of water bodies in areas filled with mangrove and mudflats is challenging due to the similarities of the spectral response of these surfaces with the water (Bishop-Taylor et al., 2019). To solve this problem, a wide range of different water delineation indexes from the literature were calculated using the raster calculator tool from the software QGIS 3.22, looking for the most capable in determining the difference between the surfaces.

Those indexes are: (i) Normalized difference water index (NDWI) proposed by McFeeters (1996); (ii) Modified normalized difference water index (MNDWI) proposed by Xu (2006); (iii) New water index (NWI) proposed by Silio-Calzada et al. (2017) specifically for shallow lakes detection in the Pantanal region but for Landsat imagery; (iv) Automated water extraction index for shadow areas (AWEI$_{sh}$) proposed by Feyisa et al. (2014), also for Landsat

imagery; (v) Sentinel water index (SWI) proposed by Jiang et al. (2021), tailored specifically for Sentinel-2 imagery.

Most of these indexes were defined for use with Landsat data in mind, however Sentinel-2 data is capable of measuring the reflectance of bands with similar wavelengths which could be used to calculate those indexes (Bhangale et al., 2020; Bijeesh et al., 2020; Jiang et al., 2021). For the ease of understanding, the Table 3 shows the correlation between each band in Landsat 5 TM and Sentinel-2.

Due to the limitation of the spatial resolution of the SWIR1 and SWIR2 bands, a 20 meters spatial resolution was chosen for the calculation of the indexes to avoid pansharpening those bands and changing their original reflectance.

Table 3 - Sentinel-2 bands and their respective correlated bands from Landsat 5 TM (Gatti-Bertolini, 2013; USGS, 2018)

| Satellite | Band | Central Wavelength (μm) | Resolution (m) | Abbreviation | Satellite | Band | Wavelength (μm) | Resolution (m) |
|---|---|---|---|---|---|---|---|---|
| Sentinel-2 MSI | B2 - Blue | 0,492 | 10 | $\rho_{Blue}$ | Landsat 5 TM | B1 - Blue | 0,45 – 0,52 | 30 |
| | B3 - Green | 0,559 | 10 | $\rho_{Green}$ | | B2 - Green | 0,52 – 0,60 | 30 |
| | B4 -Red | 0,664 | 10 | $\rho_{Red}$ | | B3 - Red | 0,63 – 0,69 | 30 |
| | B8A - Red edge | 0,864 | 20 | $\rho_{NIR}$ | | B4 - Near-infrared | 0,76 – 0,90 | 30 |
| | B11 - SWIR1 | 1,613 | 20 | $\rho_{SWIR1}$ | | B5 - Near-infrared | 1,55 – 1,75 | 30 |
| | B12 - SWIR2 | 2,202 | 20 | $\rho_{SWIR2}$ | | B7 - Mid-infrared | 2,08 – 2,35 | 30 |

### 3.3.1. NDWI

The NDWI index was calculated using equation 2, proposed by McFeeters (1996), to estimate open water in the region. This index ranges from -1 (land) to 1 (water) and uses the visible green and the near-infrared (NIR) ratios to separate water pixels based on water's high reflectance of visible green and low reflectance of NIR. As this index was initially proposed for use on Landsat 5 data, the green band and the near-infrared band can be correlated to the green band (band 3 of the Sentinel-2 data) and the near-infrared band (band 8 of the Sentinel-2 data)

from the Sentinel-2 satellite (Jiang et al., 2021), which are represented as $\rho_{Green}$ and $\rho_{NIR}$ in the formula respectively.

$$NDWI = \frac{\rho_{Green} - \rho_{NIR}}{\rho_{Green} + \rho_{NIR}} \tag{2}$$

### 3.3.2. MNDWI

The MNDWI index was calculated using equation 3, proposed by Xu (2006), to estimate open water in the region. This index is a modification of the one constructed by McFeeters (1996) and utilize a similar green band but instead of the near-infrared one it applies a middle-infrared which has wavelength similar to the SWIR1 band of Sentinel-2. Therefore band 11 can be used as the middle-infrared component proposed by Xu (2006) and is represented as $\rho_{SWIR1}$ in the MNDWI equation.

$$MNDWI = \frac{\rho_{Green} - \rho_{SWIR1}}{\rho_{Green} + \rho_{SWIR1}} \tag{3}$$

### 3.3.3. NWI

The NWI index was calculated using equation 4, proposed by Silio-Calzada et al. (2017), to estimate open water in the region. This index was proposed specifically for water detection in the Pantanal region using Landsat imagery. For its application the Landsat 5 visible bands 1, 2, 3, 4, 5 and 7 were correlated to the Sentinel-2 visible bands 2, 3, 4, 8, 11 and 12 respectively.

$$NWI = \frac{(\rho_{Blue} + \rho_{Green} + \rho_{Red}) - (\rho_{NIR} + \rho_{SWIR1} + \rho_{SWIR2})}{(\rho_{Blue} + \rho_{Green} + \rho_{Red}) + (\rho_{NIR} + \rho_{SWIR1} + \rho_{SWIR2})} \tag{4}$$

### 3.3.4. AWEI$_{sh}$

The AWEI$_{sh}$ index was calculated using equation 5, proposed by Feyisa (2014), to estimate open water in the region. The index was produced for use with Landsat 5 data, therefore similar bands from Sentinel-2 are used instead.

15

$$AWEI_{sh} = \rho_{Blue} + 2{,}5 \times \rho_{Green} - 1{,}5(\rho_{NIR} + \rho_{SWIR}) - 0{,}25 \times \rho_{SWIR2} \qquad (5)$$

### 3.3.5. SWI

The SWI index was calculated using equation 6, proposed by Jiang (2021), to estimate open water in the region. This index was made to better delineate bodies of water when using Sentinel-2 imagery since most of the indexes in the literature with this objective are built with other sensors data in mind. Because of this, it uses the band 5, vegetation red edge, that is denoted as $\rho_{VRE1}$ in the equation bellow.

$$SWI = \frac{\rho_{VRE1} - \rho_{SWIR2}}{\rho_{VRE1} + \rho_{SWIR2}} \qquad (6)$$

### 3.3.6. Otsu's algorithm thresholding

Otsu's threshold method is an efficient, widely used image binarization algorithm that distinguish objects and background using the maximum variance between them. When the pixels values of a determined image can be separated in two categories, Otsu's algorithm can determine the optimal threshold that is capable to distinguishing them (Otsu, 1979). This algorithm has been widely used for the automatic delineation of water bodies in remote sensing (Sekertekin, 2019).

Histograms with the frequency distribution for each index were produced using QGIS 3.22 and analyzed. Then, the Otsu's algorithm for image thresholding was applied for each index. For this, a python script was developed using the OpenCV library (Bradski-Kaehler, 2008) to import and convert the images to grayscale and then calculate the optimal threshold using the algorithm.

To use the Otsu's algorithm, it is necessary a grayscale 8-bit integer image, which can store values ranging from 0 to 255. In order to convert the float 32-bit images resulting from the index calculation an equation was applied to each pixel of the index images aiming to preserve their distribution while changing their values to range between 0 and 255. Equation 7 was applied for most of the indexes, NDWI, MNDWI, NWI and SWI because of their range between -1 and 1. While Equation 8 was applied to the AWEIsh index due to its wider range of values. In both equations $P_o$ refers to the original value of the pixel while $P_n$ refers to the new value of the pixel.

$$P_n = (P_o + 1) \times 100 \qquad (7)$$

$$P_n = \frac{(P_o + 10.000)}{100} \qquad (8)$$

After the threshold calculation, the resulting pixel value was used in equation 7 or 8 to get back the original pixel value to be used as threshold in the calculated indexes. The results can be visualized in table 4. Finally, a water extraction map was constructed for each index calculated using this threshold, highlighting the open water surface defined by each one.

Table 4 - Optimal threshold defined by the Otsu's algorithm for each index used.

| Index | Otsu's Algorithm Threshold |
|---|---|
| NDWI | -0,6 |
| MNDWI | -0,38 |
| NWI | -0,53 |
| AWEIsh | -4.272 |
| SWI | 0 |

### 3.4. Accuracy Assessment

To assess the quality of the delineation of each index for the region, they were compared in the high-water season of 2017 where high resolution (1,2 meters spatial resolution) satellite images from Maxar were available through ArcGIS Online. A visual interpretation and a quantitative accuracy index were used to assess the accuracy of the water extraction maps created. First, they were visually compared with each other and with a true color image (TCI), a false color image (band 8 as red, band 4 as green and band 3 as blue) and a high spatial resolution image. At this step, visual effects which can quickly appraise the performance of the method such as continuity, smoothness and salt and pepper effect were observed.

For the quantitative accuracy, 100 sample points were randomly generated (Figure 9). Then, through photointerpretation of true color images, false color images and high-resolution imagery they were classified, 21 water sample points and 79 non-water sample points were identified (Figure 9). This data was then used as the ground reference points for the accuracy evaluation of the indexes.
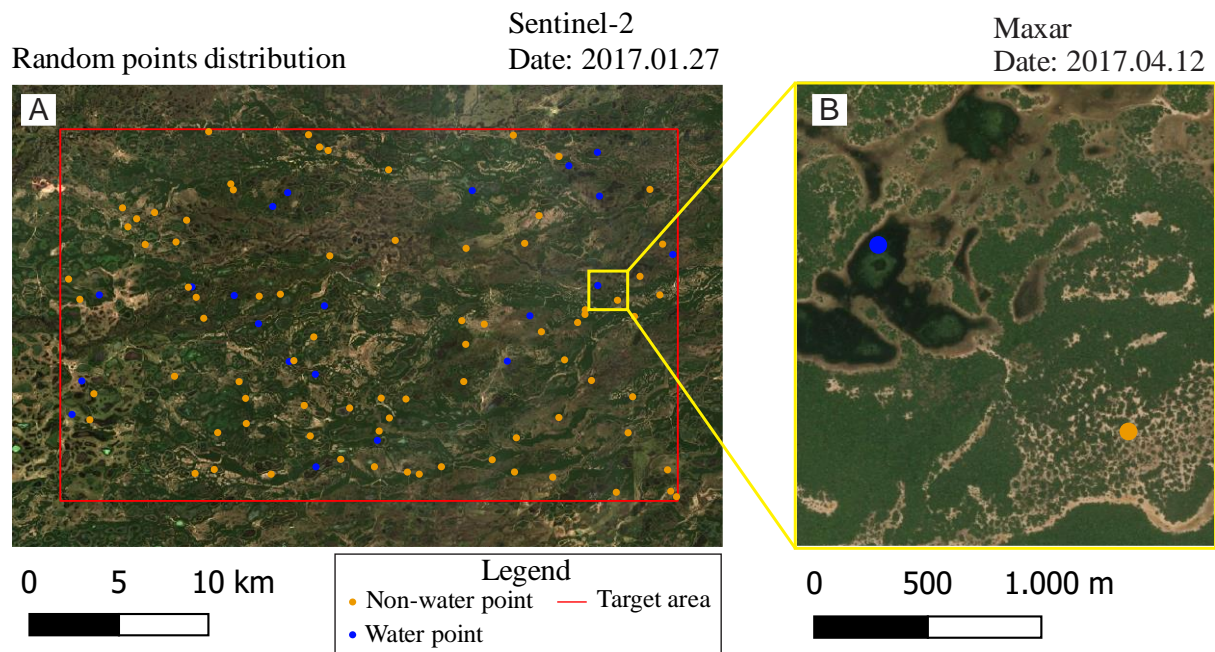
Figure 9 - A) Distribution of the random points generated for the target area and their respective classification, in the background a true color image from Sentinel-2. B) Detailed view of the highlighted area in Figure 9A showing two random points in the higher resolution Maxar true color image.

To evaluate the accuracy of these images, they should be compared to the reference random points that are presumed to be correct (Foody, 2002). The result of this comparison should be a confusion matrix, pointing out the errors that the classification presented when compared to the referential data (Congalton, 1991). From this confusion matrix a Kappa index can be calculated and it will be used to evaluate the quality of the resulting classification according to Landis and Koch (1977) evaluation criteria (Table 5).

Table 5 - Relative strength of agreement associated with the Kappa index (Landis-Koch, 1977).

| Kappa Index | Strength of Agreement |
|---|---|
| < 0 | Poor |
| 0 - 0,2 | Slight |
| 0,21 - 0,4 | Fair |
| 0,41 - 0,6 | Moderate |
| 0,61 - 0,8 | Substantial |
| 0,81 - 1 | Almost Perfect |

The index images were reclassified using the threshold calculated by the Otsu algorithm creating binary images, classifying the pixels as water pixels or non-water pixels. Then, using Orfeo ToolBox confusion matrix tool (Grizonnet et al., 2017), a confusion matrix was built and a Kappa index was calculated.

After this analysis, most of the indexes were abandoned and the AWEIsh was chosen as the most fitting index for the region and will be used further on this work.

### 3.5. Thematical maps time series and landcover change

At last, using the AWEIsh index and a -4.272 threshold, a thematic map for each year high water and low water was built in the WGS 84 / UTM zone 21S (EPSG 32721) projected coordinate system with a 1:400.000 scale. To evaluate the accuracy of these maps a similar method to the accuracy evaluation of the indexes was applied. First, 100 random points were generated for each map and then through photointerpretation of true color images and false color images they were classified as water or non-water. Later on, using Orfeo ToolBox confusion matrix tool (Grizonnet et al., 2017), a confusion matrix was built and a kappa index calculated. They were then compared and analyzed to assess the evolution of the hydrography of the water bodies of the target region.

To better understand and measure the changes in water surface area between the seasons and the years, the total water surface and the differences between the seasons in each year were measured. For this, the land cover change tool from the Semi-Automatic Classification Plugin (Congedo, 2021) for QGIS was utilized. The result provided the number of pixels and area for 4 different classes: (i) water unchanged, (ii) non-water unchanged, (iii) non-water to water and (iv) water to non-water.

# 4. RESULTS AND DISCUSSION

## 4.1. Index accuracy evaluation

Due to the complex nature of the region, the application of five different indexes was analyzed for the 2017 high water data of the time series. The results for each index and their respective threshold calculated by the Otsu's algorithm can be visualized in a frequency histogram (Figure 10). It is possible to observe that each index accounted for a different total number of pixels classified as water.

From the histograms (Figure 10) we can predict that the SWI index oversampled the pixels and detected other features as water. Conversely, the MNDWI index sampled too few pixels and failed to delineate some bodies of water (Figures 10 and 11).

Five water extraction maps were created (Figure 11) using the geographic projection WGS 84 / UTM zone 21S (EPSG 32721) with a scale of 1:500.000. The difference in the total water surface between the different indexes is even more evident in those maps mostly in the SWI and MNDWI maps that showed a much larger water surface and a much smaller water surface respectively (Figure 11).

It is also possible to observe problems with continuity, smoothness and salt and pepper effect in some indexes (Figures 11 and 12). The NDWI, MNDWI and NWI indexes showed regularly problems with continuity and salt and pepper effect, as seen on figure 12, while the AWEIsh index had a better result overall, showing problems but in more isolated areas. On the other hand, the SWI index oversampled heavily and even though it didn't show much problems with continuity and smoothness it recognized most of the vegetation as water (Figure 12).

All of the indexes had some difficulty to distinguish wet soil and water (Figure 12), while the NDWI also identified regular soil as water. The NDWI and NWI indexes presented salt and pepper effect in heavily vegetated areas, while the AWEIsh index had difficulty to distinguish heavily vegetated water (Figure 12).

Finally, the accuracy assessment performed by confusion matrix (Table 6) and Kappa index (Table 7) determined that the most fitting index for the area is the AWEIsh. With a Kappa index of 0,87 it is considered by the Landis and Koch (1977) strength of agreement table as an almost perfect correlation.
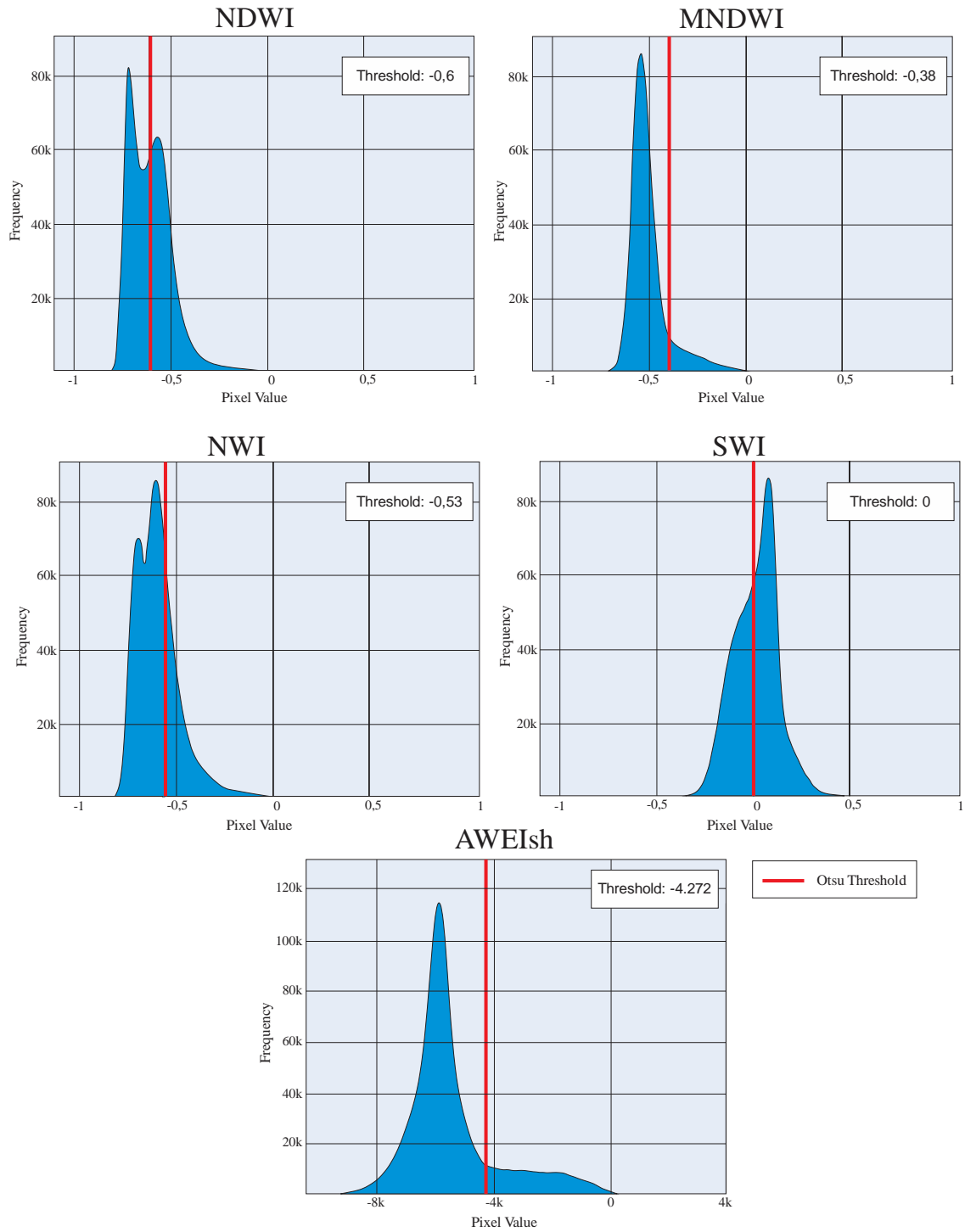
Figure 10 - Frequency histogram for each of the five water delineation index evaluated, in red the threshold calculated by the Otsu's algorithm.
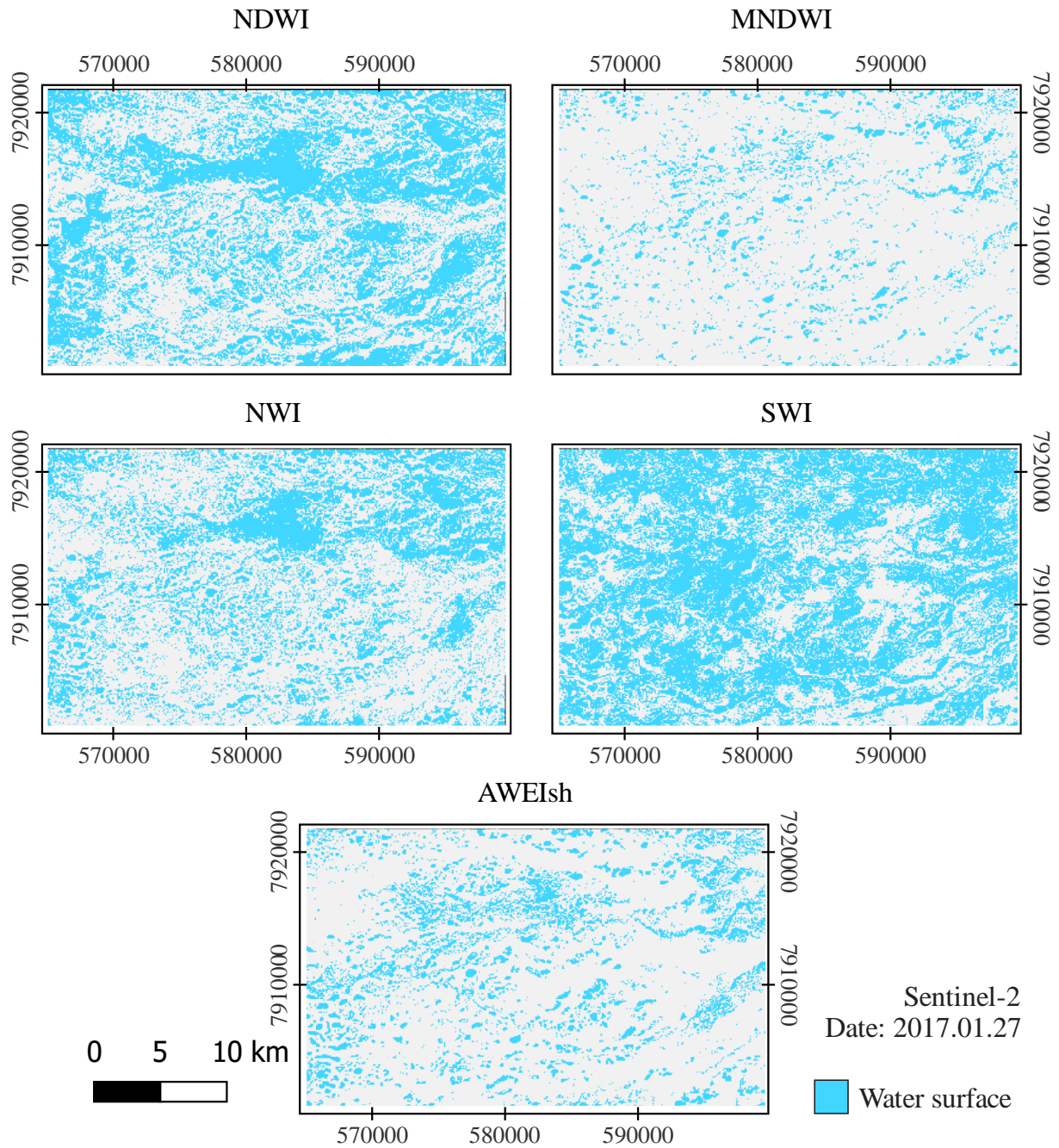
Figure 11 - Water extraction map for each of the evaluated indexes, constructed based on Sentinel-2 sensed data from 2017.01.27. Geographic projection WGS 84 / UTM zone 21S (EPSG 32721), scale 1:500.000.
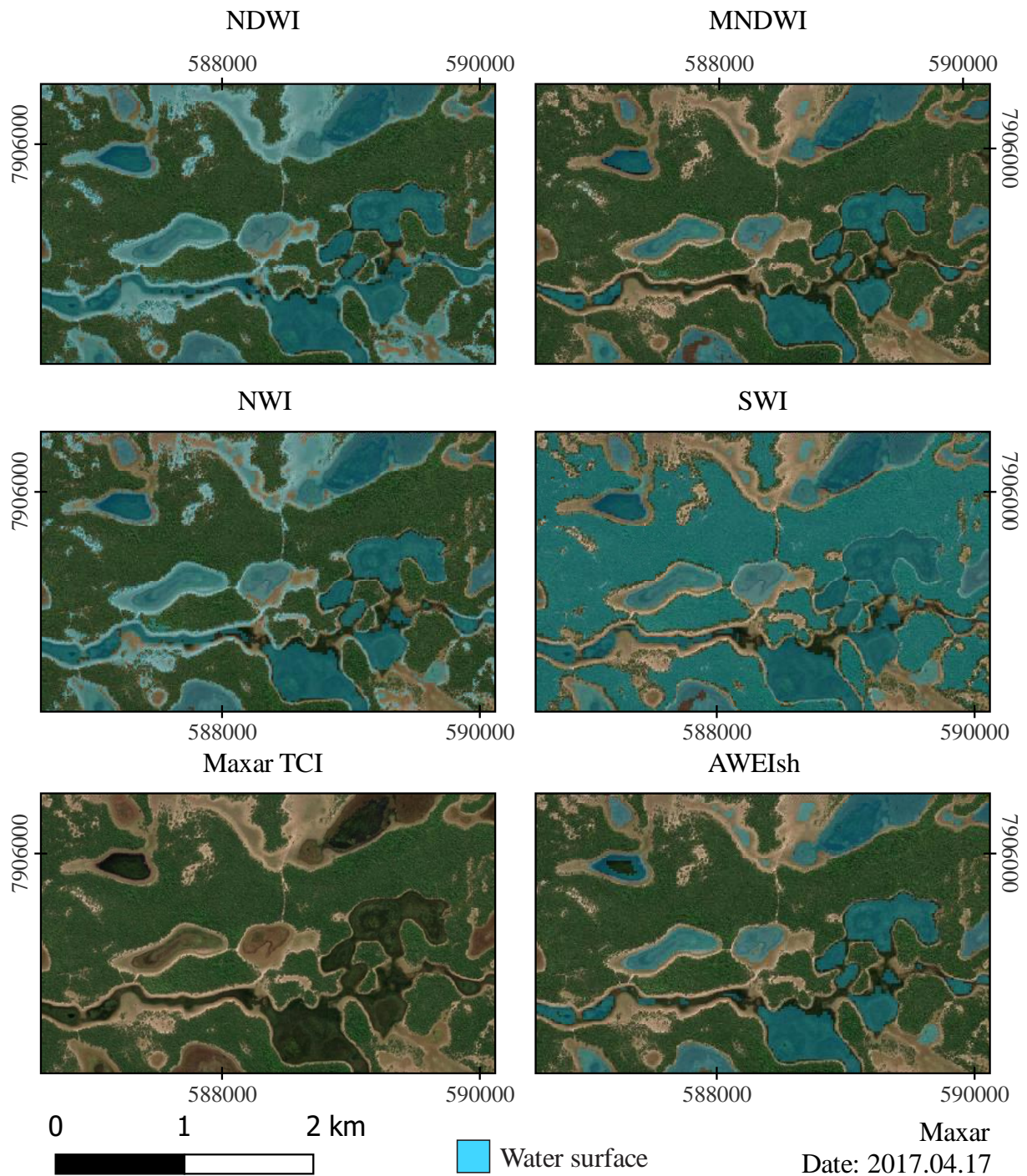
Figure 12 - Detailed observation of the indexes calculated for the high water of 2017. In the background high-resolution imagery from Maxar. Maps in the scale 1:50.000, geographic projection WGS 84 / UTM zone 21S (EPSG 32721).

Table 6 - Confusion matrix for each index using the threshold determined by the Otsu's algorithm and the random points classified as ground truth.

| NDWI | Ground Truth | |
|---|---|---|
| **Classification** | Water | Non-water |
| Water | 18 | 3 |
| Non-water | 30 | 49 |

*Classified by Index*

| MNDWI | Ground Truth | |
|---|---|---|
| **Classification** | Water | Non-water |
| Water | 12 | 9 |
| Non-water | 1 | 78 |

*Classified by Index*

| NWI | Ground Truth | |
|---|---|---|
| **Classification** | Water | Non-water |
| Water | 18 | 3 |
| Non-water | 19 | 60 |

*Classified by Index*

| SWI | Ground Truth | |
|---|---|---|
| **Classification** | Water | Non-water |
| Water | 19 | 2 |
| Non-water | 37 | 42 |

*Classified by Index*

| AWEIsh | Ground Truth | |
|---|---|---|
| **Classification** | Water | Non-water |
| Water | 19 | 2 |
| Non-water | 2 | 77 |

*Classified by Index*

Table 7 - Kappa index, overall accuracy and strength of agreement for each analyzed water extraction index.

| Water Extraction Index | Kappa Index | Overall Accuracy | Strength of Agreement (Landis-Koch, 1977) |
|---|---|---|---|
| NDWI | 0,32 | 0,67 | Fair |
| MNDWI | 0,64 | 0,9 | Substantial |
| NWI | 0,48 | 0,78 | Moderate |
| SWI | 0,27 | 0,61 | Fair |
| AWEIsh | 0,87 | 0,96 | Almost Perfect |

*4.2. Time series*

Figures 13, 14, 15, 16, 17, 18 and 19 show two maps of water surface delineation for each of the seven years analyzed. All the maps are presented in geographic projection WGS 84

/ UTM zone 21S (EPSG 32721) and scale 1:400.000. In the background of each map is a true color image of the dataset used to produce the water extraction data.



Figure 13 - Water extraction maps for the high and low water stages of the year 2016.

Figure 14 - Water extraction maps for the high and low water stages of the year 2017.

Figure 15 - Water extraction maps for the high and low water stages of the year 2018.

Figure 16 - Water extraction maps for the high and low water stages of the year 2019.

Figure 17 - Water extraction maps for the high and low water stages of the year 2020.
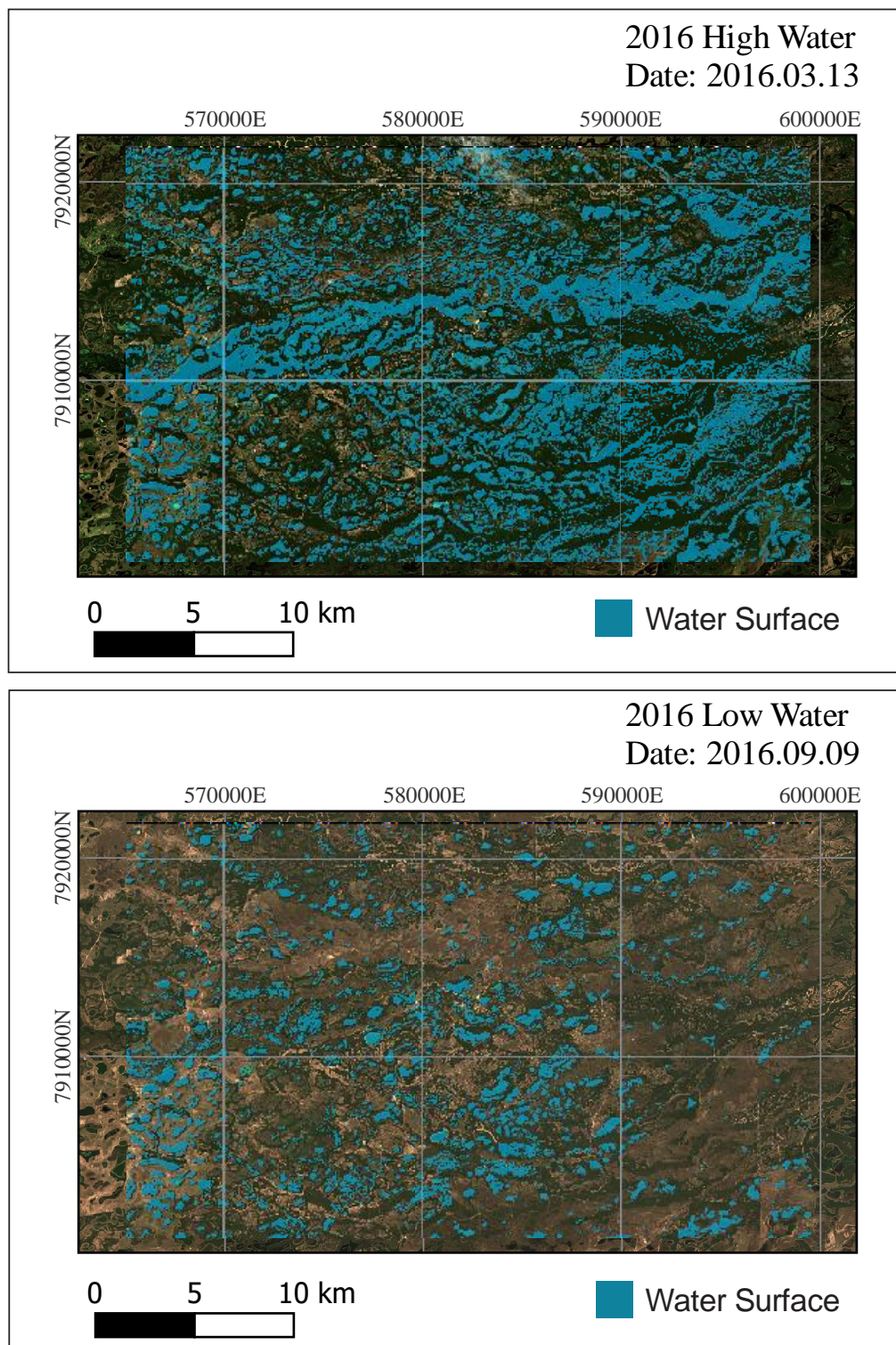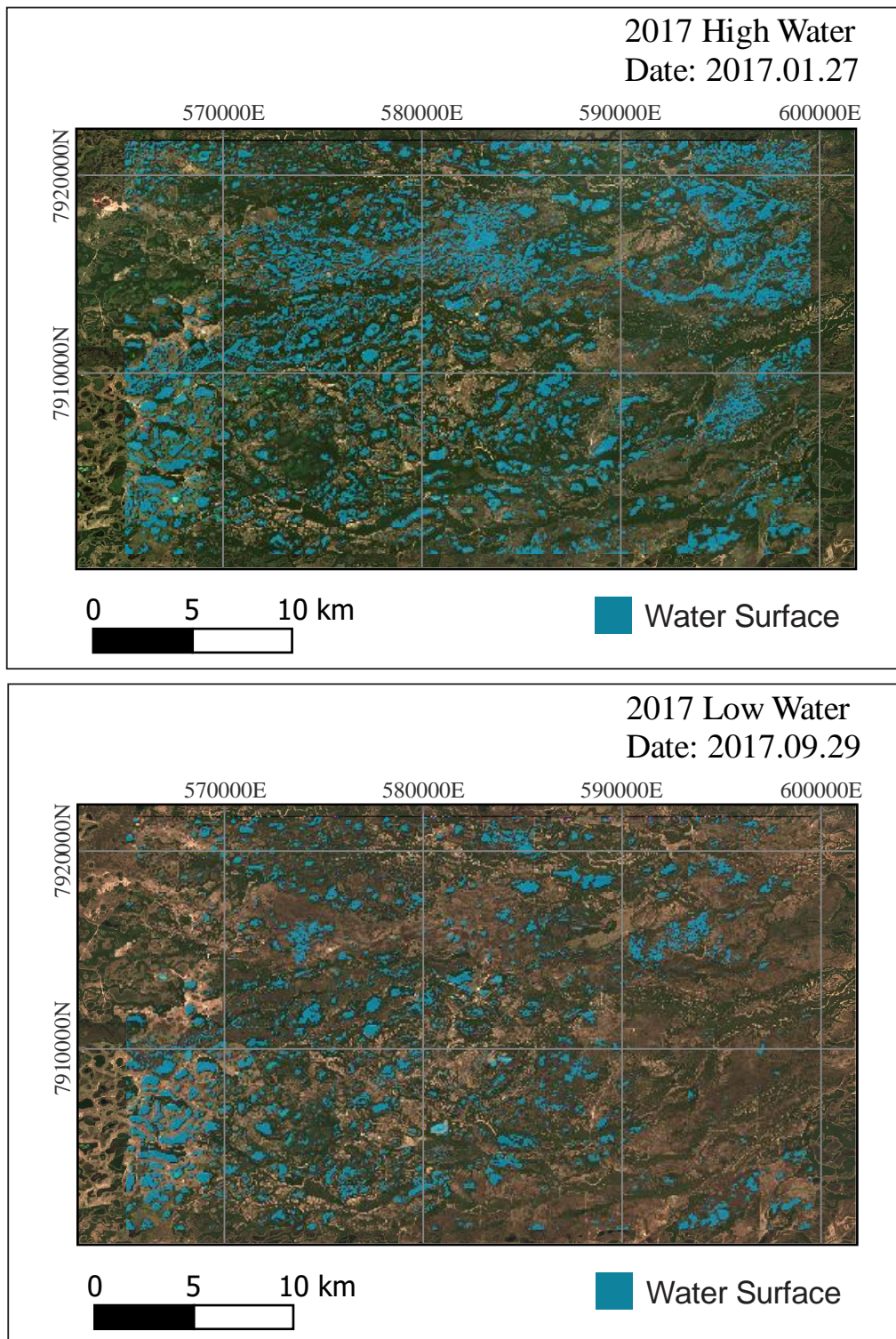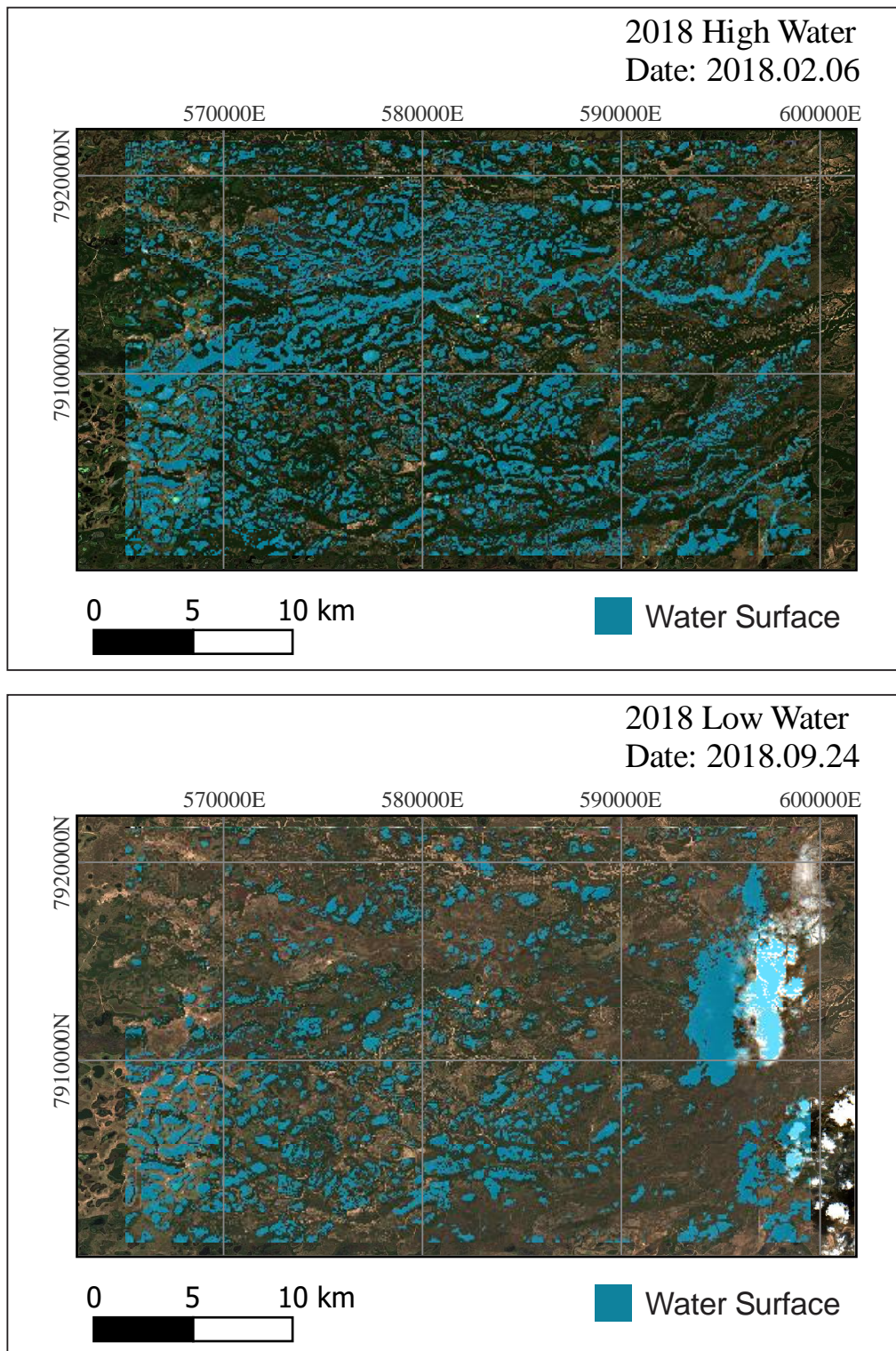
Figure 18 - Water extraction maps for the high and low water stages of the year 2021.
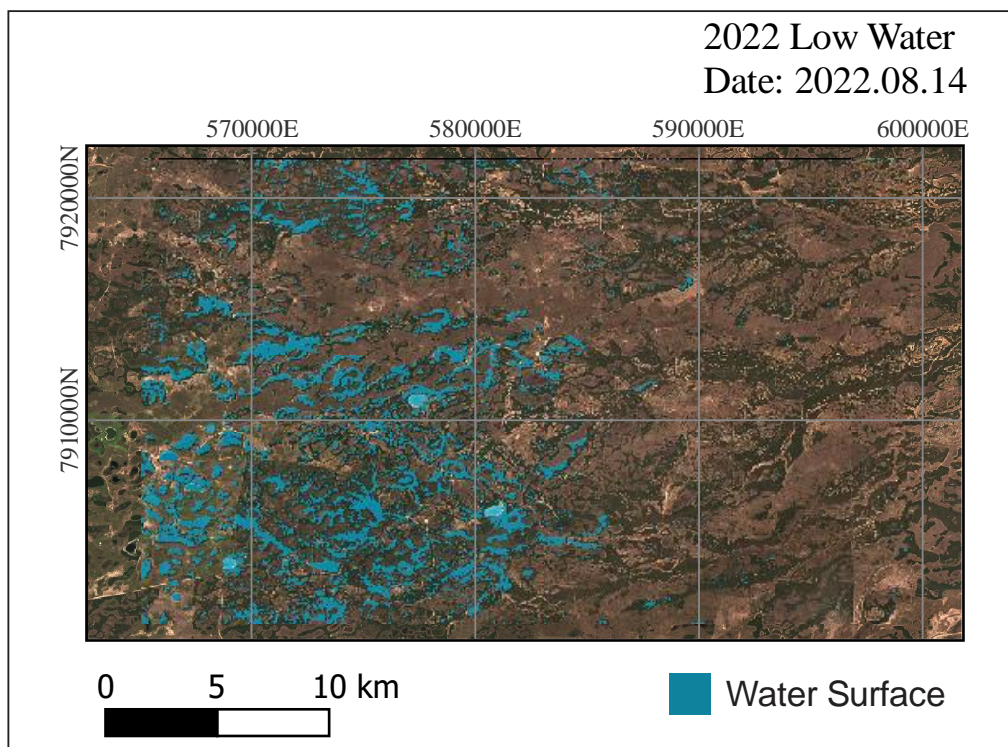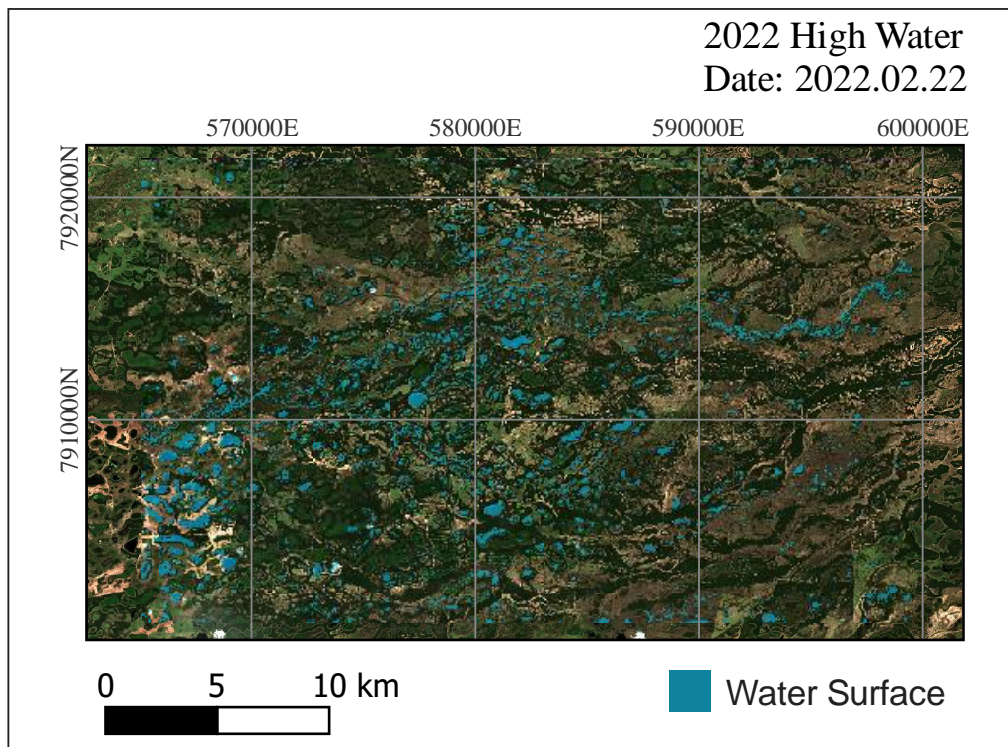
Figure 19 - Water extraction maps for the high and low water stages of the year 2022.
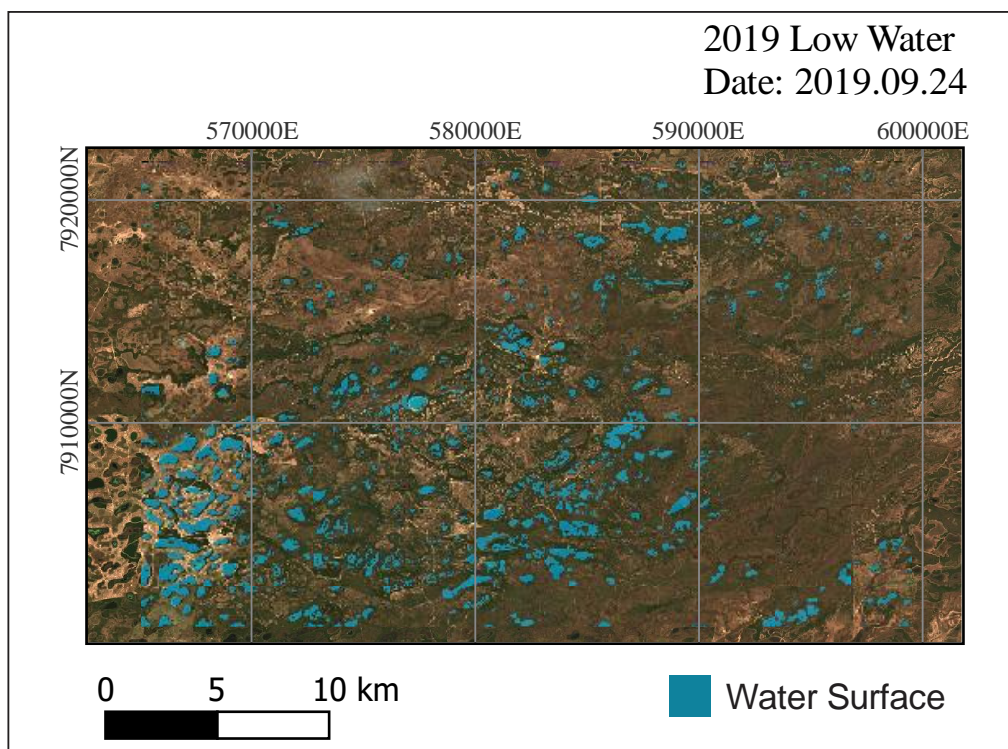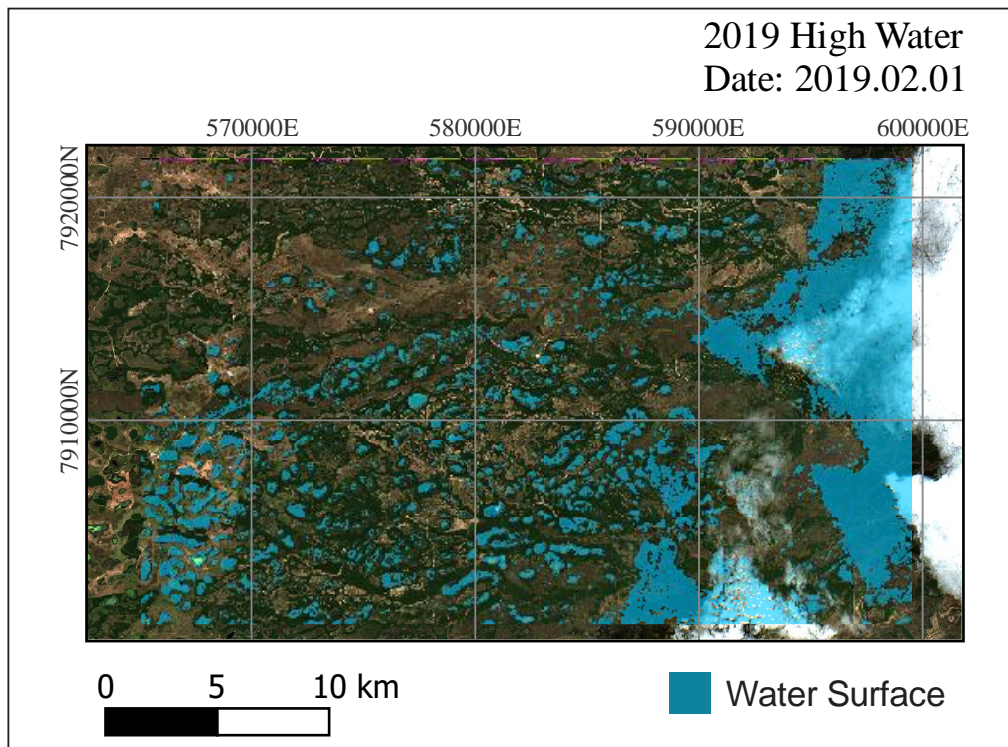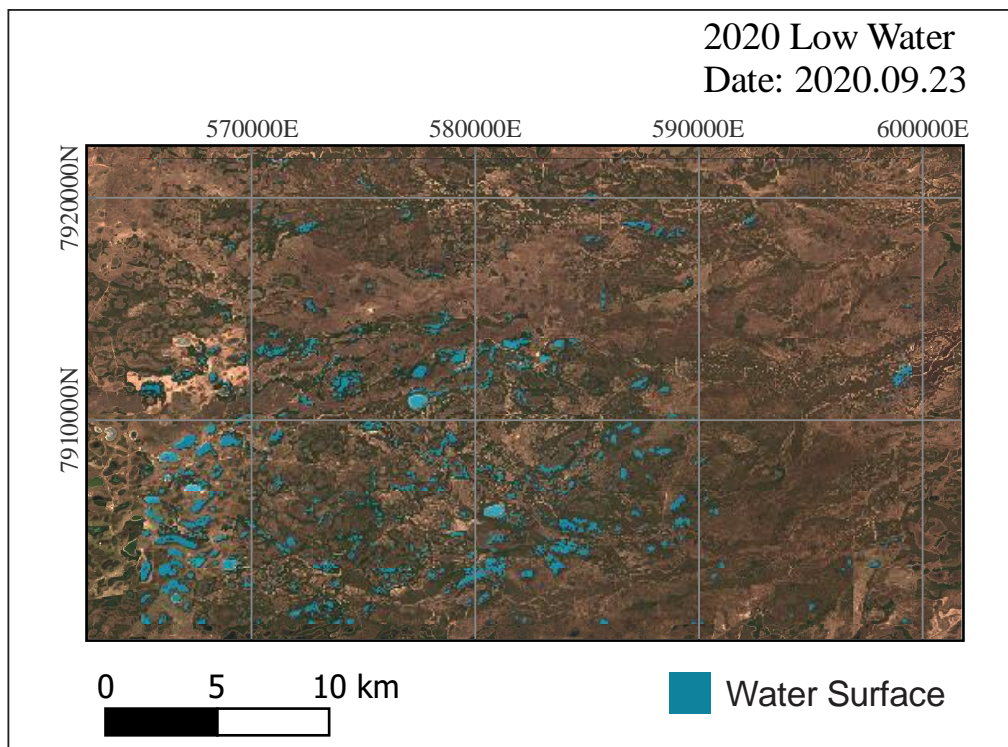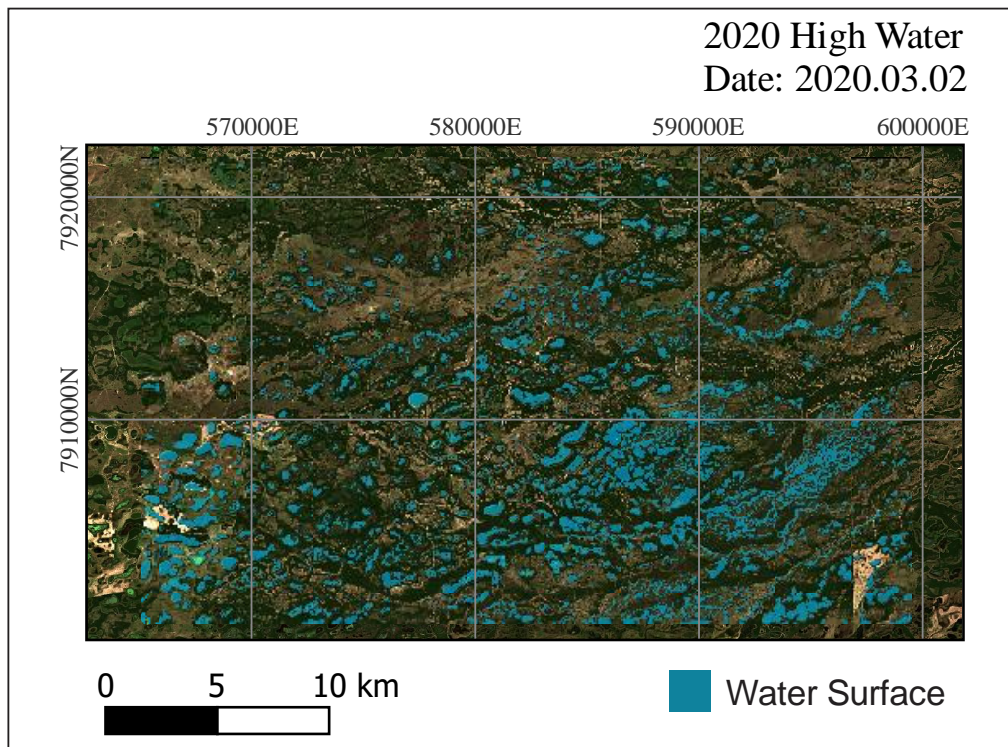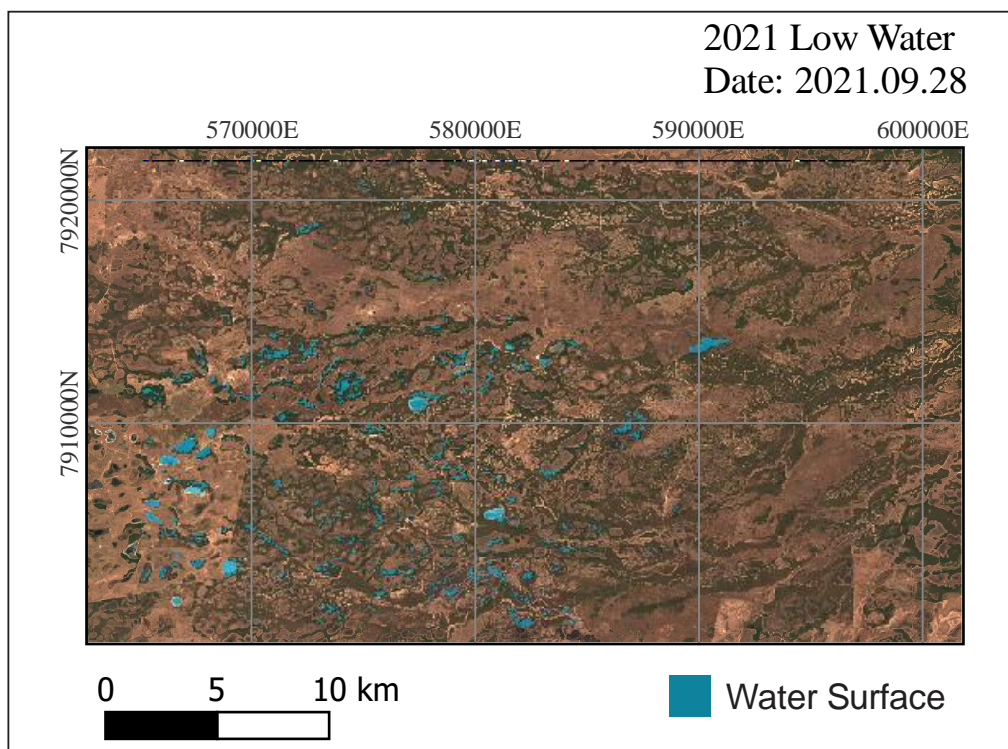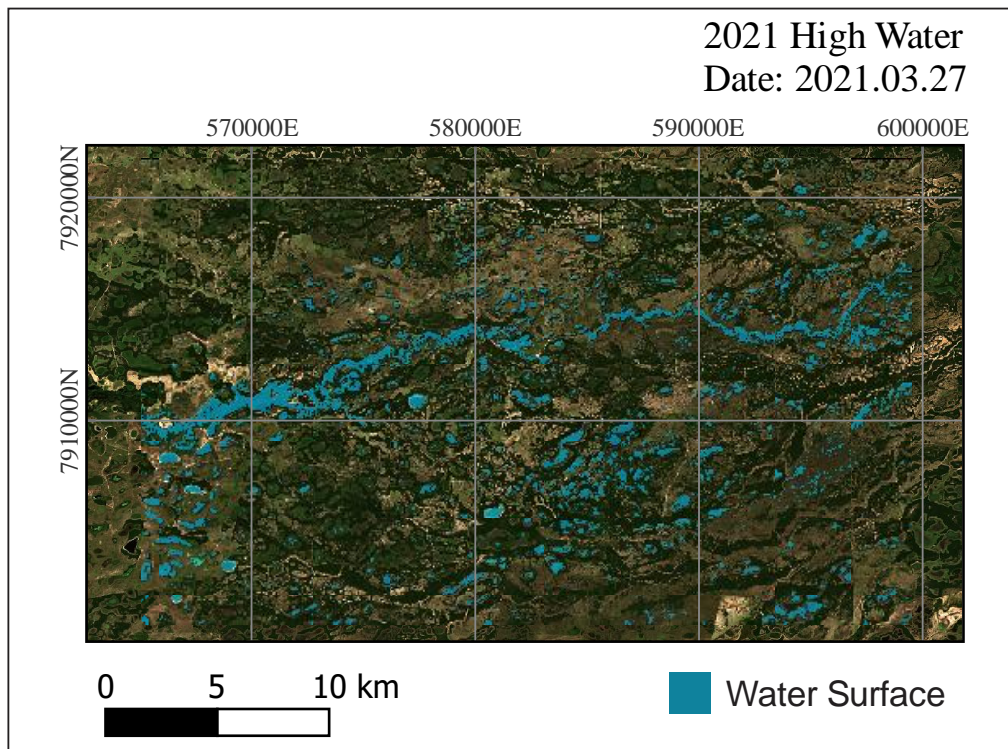
At first glance, it is easy to visualize the dramatic difference of water surface between seasons. It is also possible to observe that there was a substantial decrease in water surface from the low water stage of 2020 onwards. the high water stage has seen a decrease since the year of 2018 but not as dramatic as the one observed in the dry season.

The volume of oversampled pixels is not constant, as it is possible to observe that certain images have a much higher volume of wrongly extracted pixels. This is especially visible at the low water of 2022 (Figure 19), where a lot of vegetation pixels were detected as water by the index. This problem is mostly present in the images of the low water stage.

### 4.3. Water surface accuracy evaluation

Overall, the water surface extraction images have a good accuracy and most of them were classified as an almost perfect correlation (Table 9) by the Landis-Koch (1977) strength of agreement method. The confusion matrixes show that there is a small undersampling of water pixels at the high water stage and its mostly visible at the 2016 high water (Table 8). There is also a small oversampling of water pixels that is mostly visible at the 2022 low water and at the cloudy areas from 2019 high water and 2018 low water (Table 8).

Table 8 – Confusion matrix for each stage throughout the years analyzed using the random points classified as ground truth.

| 2016 – High Water | | Ground Truth | |
|---|---|---|---|
| | Classification | Water | Non-water |
| Classified by Index | Water | 27 | 2 |
| | Non-water | 5 | 66 |

| 2016 – Low Water | | Ground Truth | |
|---|---|---|---|
| | Classification | Water | Non-water |
| Classified by Index | Water | 9 | 2 |
| | Non-water | 0 | 89 |

| 2017 – High Water | | Ground Truth | |
|---|---|---|---|
| | Classification | Water | Non-water |
| Classified by Index | Water | 19 | 2 |
| | Non-water | 2 | 77 |

| 2017 – Low Water | | Ground Truth | |
|---|---|---|---|
| | Classification | Water | Non-water |
| Classified by Index | Water | 10 | 2 |
| | Non-water | 4 | 84 |

| 2018 – High Water | | Ground Truth | |
|---|---|---|---|
| | Classification | Water | Non-water |
| Classified by Index | Water | 22 | 3 |
| | Non-water | 2 | 73 |

| 2018 – Low Water | | Ground Truth | |
|---|---|---|---|
| | Classification | Water | Non-water |
| Classified by Index | Water | 12 | 8 |
| | Non-water | 3 | 77 |

| 2019 – High Water | Ground Truth | |
| --- | --- | --- |
| **Classification** | Water | Non-water |
| Classified by Index — Water | 4 | 13 |
| Classified by Index — Non-water | 2 | 81 |

| 2019 – Low Water | Ground Truth | |
| --- | --- | --- |
| **Classification** | Water | Non-water |
| Classified by Index — Water | 2 | 1 |
| Classified by Index — Non-water | 1 | 96 |

| 2020 – High Water | Ground Truth | |
| --- | --- | --- |
| **Classification** | Water | Non-water |
| Classified by Index — Water | 14 | 0 |
| Classified by Index — Non-water | 3 | 83 |

| 2020 – Low Water | Ground Truth | |
| --- | --- | --- |
| **Classification** | Water | Non-water |
| Classified by Index — Water | 4 | 0 |
| Classified by Index — Non-water | 1 | 95 |

| 2021 – High Water | Ground Truth | |
| --- | --- | --- |
| **Classification** | Water | Non-water |
| Classified by Index — Water | 8 | 0 |
| Classified by Index — Non-water | 1 | 91 |

| 2021 – Low Water | Ground Truth | |
| --- | --- | --- |
| **Classification** | Water | Non-water |
| Classified by Index — Water | 1 | 0 |
| Classified by Index — Non-water | 1 | 98 |

| 2022 – High Water | Ground Truth | |
| --- | --- | --- |
| **Classification** | Water | Non-water |
| Classified by Index — Water | 8 | 1 |
| Classified by Index — Non-water | 1 | 90 |

| 2022 – Low Water | Ground Truth | |
| --- | --- | --- |
| **Classification** | Water | Non-water |
| Classified by Index — Water | 3 | 7 |
| Classified by Index — Non-water | 0 | 90 |

### 4.4. Water surface change

Seven water surface change maps were made to visualize the changes between the seasons in each year (Figures 20, 21, 22 and 23). The water surface change calculations were performed between the high water stage and low water stage of each year of the time series. Its results can be seen at table 10 or visually at figure 25.

From the water surface change maps it is possible to visualize that the larger lakes, at the southwest of the target area, rarely dry up from the wet to the dry season and mostly retain their size. Between years, however, their size did decrease and their numbers skewed from the beginning to the end of the time series. The lakes next to the center of the area suffered a decrease between seasons. Some of them even dry up completely between the high water and the low water.

Table 9 – Kappa index, overall accuracy and strength of agreement for each stage of the years analyzed.

| Image | Kappa Index | Overall Accuracy | Strength of Agreement (Landis-Koch, 1977) |
|---|---|---|---|
| 2016 - High Water | 0,83 | 0,93 | Almost Perfect |
| 2016 - Low Water | 0,89 | 0,98 | Almost Perfect |
| 2017 - High Water | 0,87 | 0,96 | Almost Perfect |
| 2017 - Low Water | 0,73 | 0,94 | Substantial |
| 2018 - High Water | 0,86 | 0,95 | Almost Perfect |
| 2018 - Low Water | 0,62 | 0,89 | Substantial |
| 2019 - High Water | 0,28 | 0,85 | Fair |
| 2019 - Low Water | 0,65 | 0,98 | Substantial |
| 2020 - High Water | 0,88 | 0,97 | Almost Perfect |
| 2020 - Low Water | 0,88 | 0,99 | Almost Perfect |
| 2021 - High Water | 0,93 | 0,99 | Almost Perfect |
| 2021 - Low Water | 0,66 | 0,99 | Substantial |
| 2022 - High Water | 0,87 | 0,98 | Almost Perfect |
| 2022 - Low Water | 0,43 | 0,93 | Fair |

The features that were affected the most between the wet and the dry season were the braided rivers. In the target area during the high water it is possible to observe one braided river that runs through the area from west to the east and splits itself in two, one to the north and one to the south. During the low water, however, this feature is almost completely dried, being one of the factors that most influences the changes in water surface area. Throughout the year these rivers suffered a dramatic decrease in their sizes.

The pixels classified as non-water to water change highlighted the oversampled problem observed in the water extraction maps (Figure 24). This problem occurs mostly on dark vegetation canopy pixels during the low water stage. It is noticeable that the pixels highlighted as non-water to water rarely represents circular or ellipsoidal shapes and have problems of continuity and smoothness. Moreover, given the nature of the region, the increase of the water surface from the high water stage to the low water stage is contradictory (DaSilva-Silva, 1995;

Junk et al., 2014) and the measuring of these pixels during the low water stage represents an issue to the method applied in this work.



Figure 20 - Water surface change maps for the years 2016 and 2017.

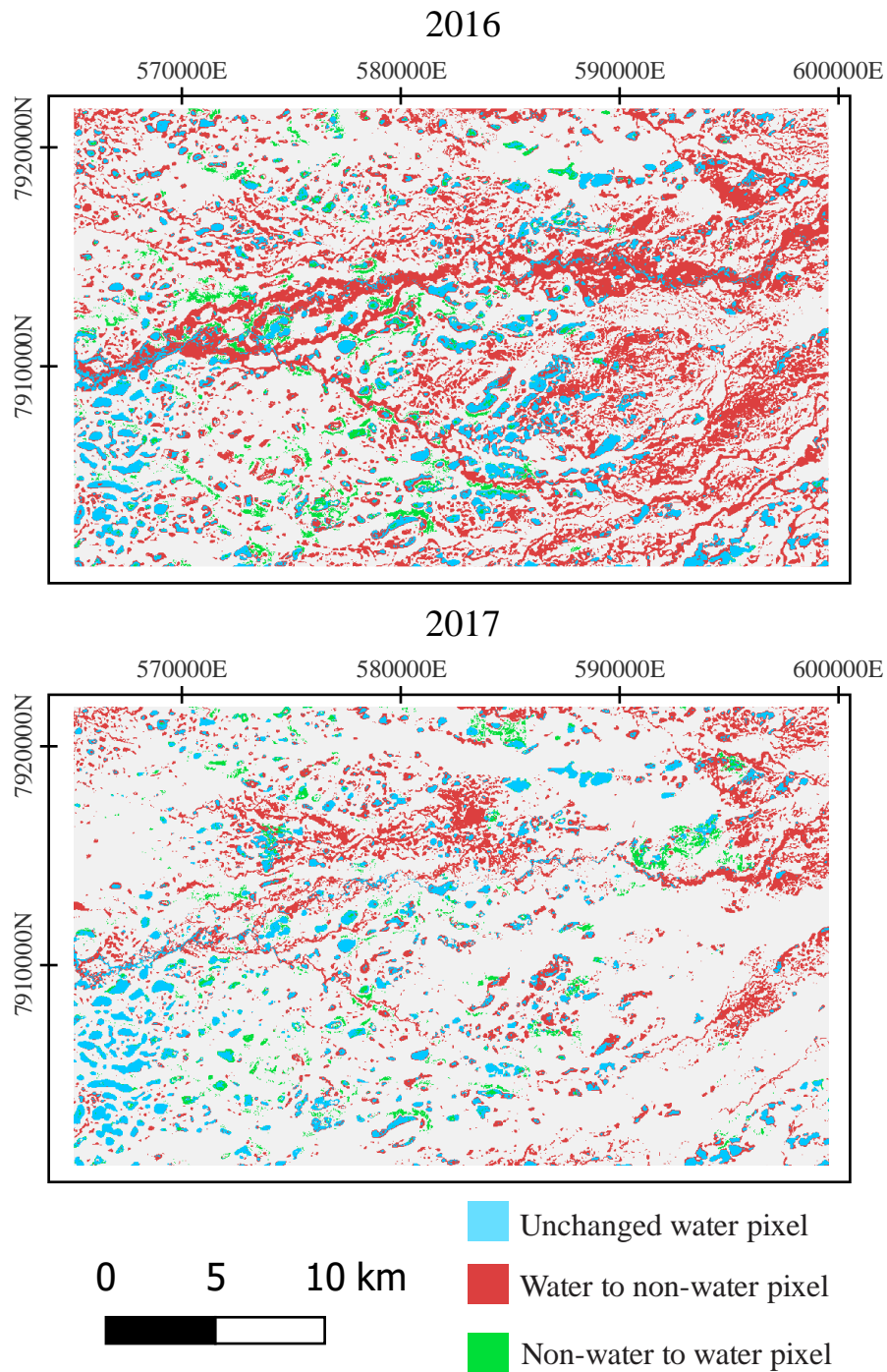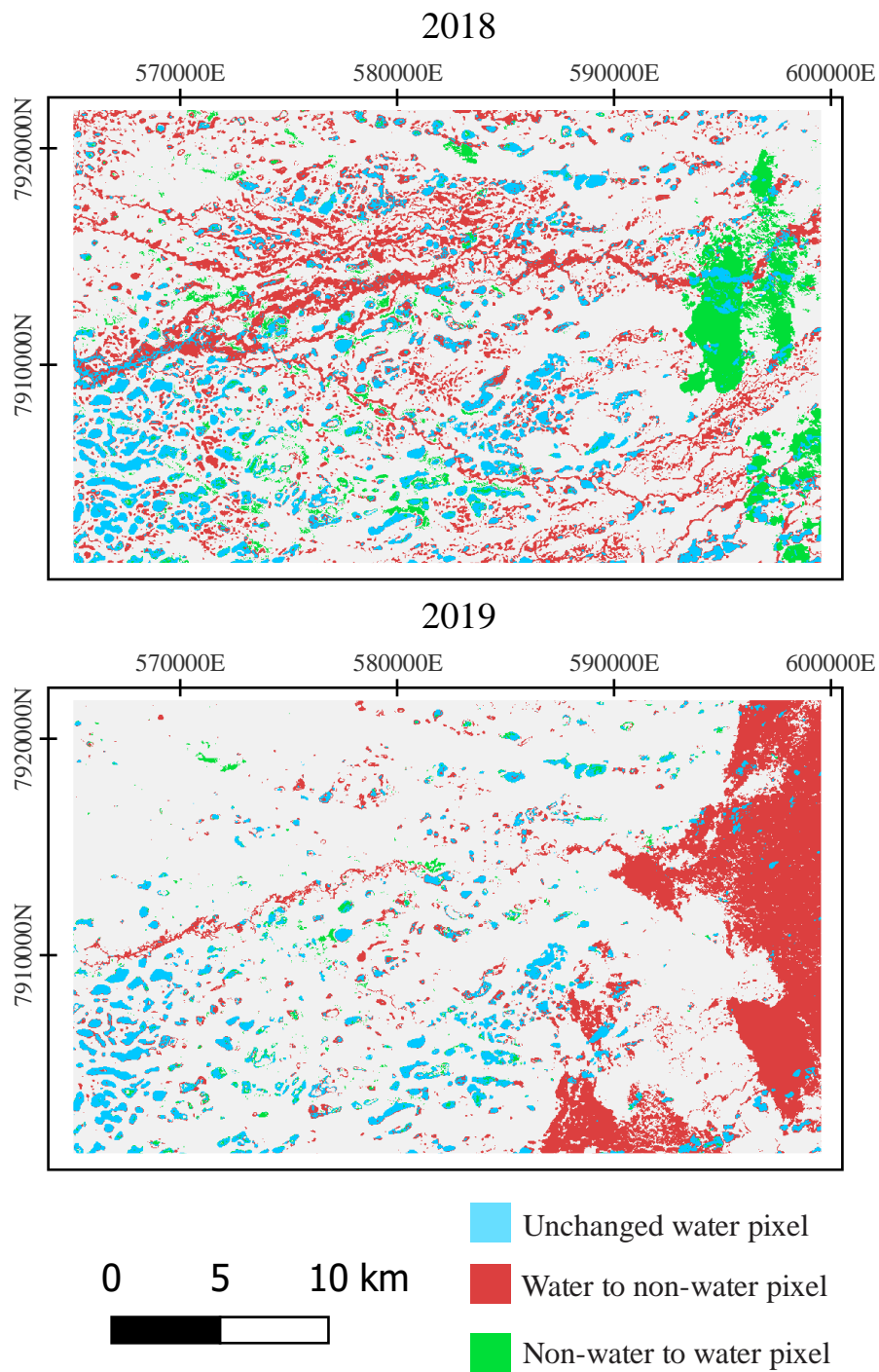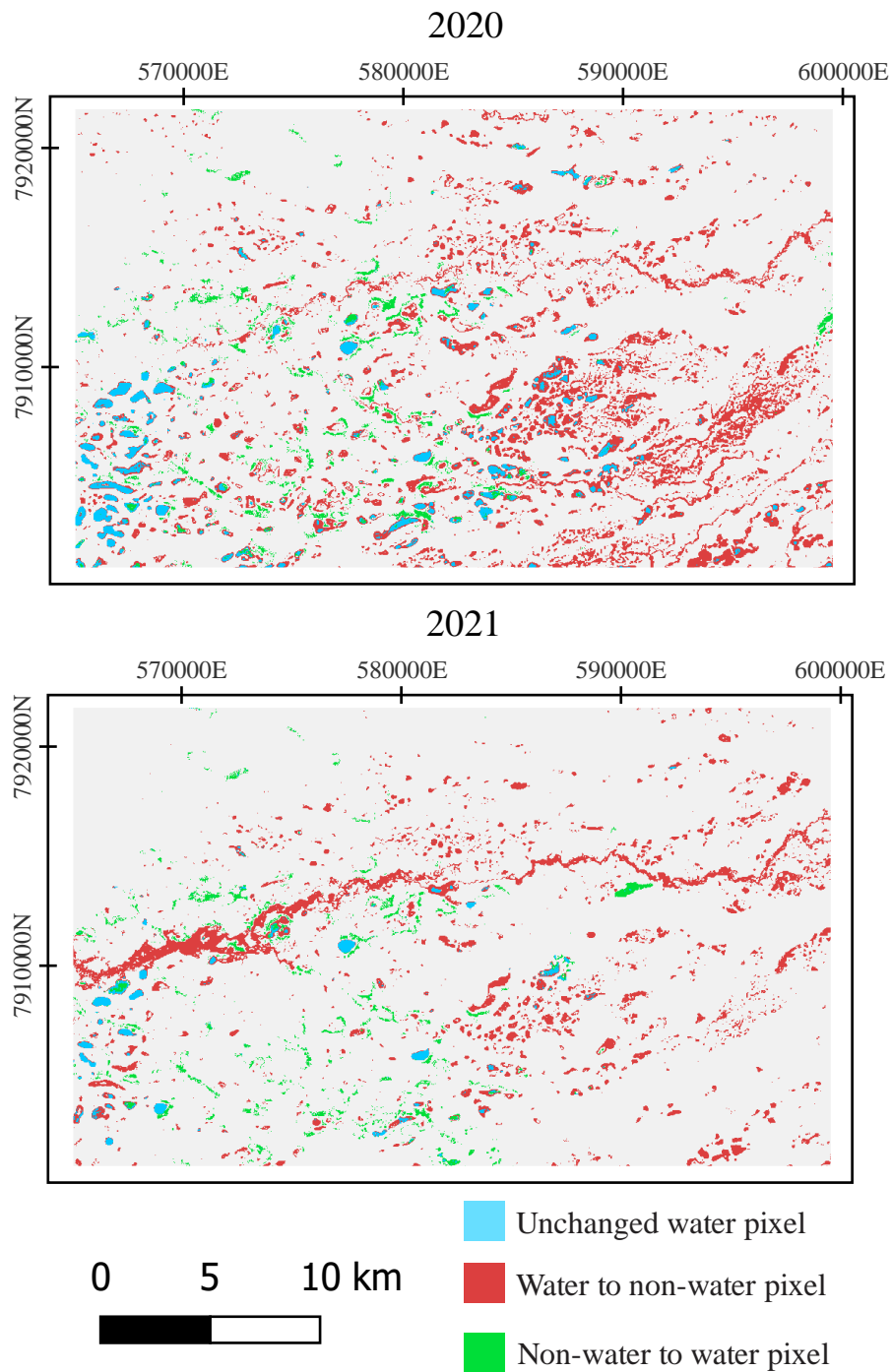Figure 21 - Water surface change maps for the years 2018 and 2019.

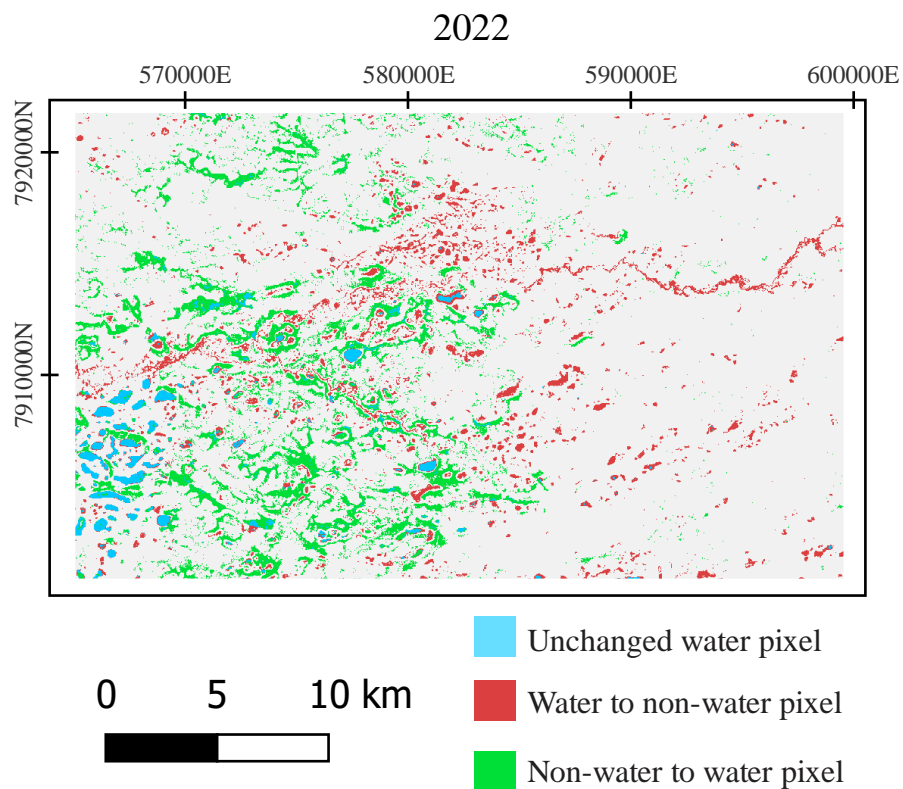Figure 22 - Water surface change maps for the years 2020 and 2021.

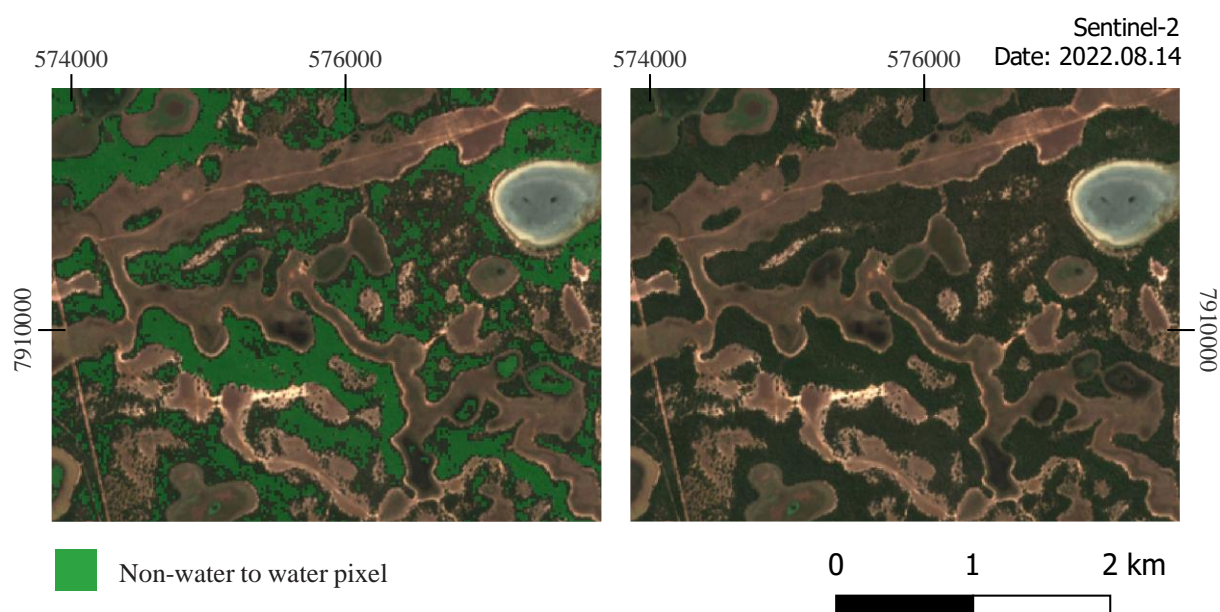Figure 23 - Water surface change map for the year 2022.



Figure 24 - Detailed visualization of the non-water to water pixels for the low water stage of 2022, in the background a Sentinel-2 true color image. Scale 1:50.000 geographic projection WGS 84 / UTM zone 21S (EPSG 32721).

To avoid the measurement of oversampled pixels of vegetation (Figure 24) during the water surface area calculation, the water surface area for the low water stage ($A_{lw}$) was calculated (Equation 9) using the water surface area from the high water stage ($A_{hw}$) of the same year minus the area occupied by the pixels that were detected as changing from water to non-water ($C_{w-nw}$) at that year by the land cover change tool. This was done assuming that new bodies of water should not appear during a dryer season with lesser water influx.

$$A_{lw} = A_{hw} - C_{w-nw} \qquad (9)$$

Table 10 - Water surface detected for the years 2016 through 2022 and their variation between the seasons.

| Year / Stage | Water Surface (km²) | Water Surface (% of total area) | Year Variance (km²) | Year Variance (% of water surface reduction) |
|---|---|---|---|---|
| 2016 High Water | 238,25 | 32,93 | 179,96 | 75,53 |
| 2016 Low Water | 58,29 | 8,06 | | |
| 2017 High Water | 127,97 | 17,69 | 83,45 | 65,21 |
| 2017 Low Water | 44,52 | 6,15 | | |
| 2018 High Water | 180,25 | 24,91 | 108,49 | 60,19 |
| 2018 Low Water | 71,76 | 9,92 | | |
| 2019 High Water | 156,50 | 21,63 | 118,43 | 75,68 |
| 2019 Low Water | 38,07 | 5,26 | | |
| 2020 High Water | 84,71 | 11,71 | 70,53 | 83,26 |
| 2020 Low Water | 14,18 | 1,96 | | |
| 2021 High Water | 46,20 | 6,38 | 42,10 | 91,13 |
| 2021 Low Water | 4,10 | 0,57 | | |
| 2022 High Water | 40,20 | 5,56 | 29,99 | 74,60 |
| 2022 Low Water | 10,21 | 1,41 | | |
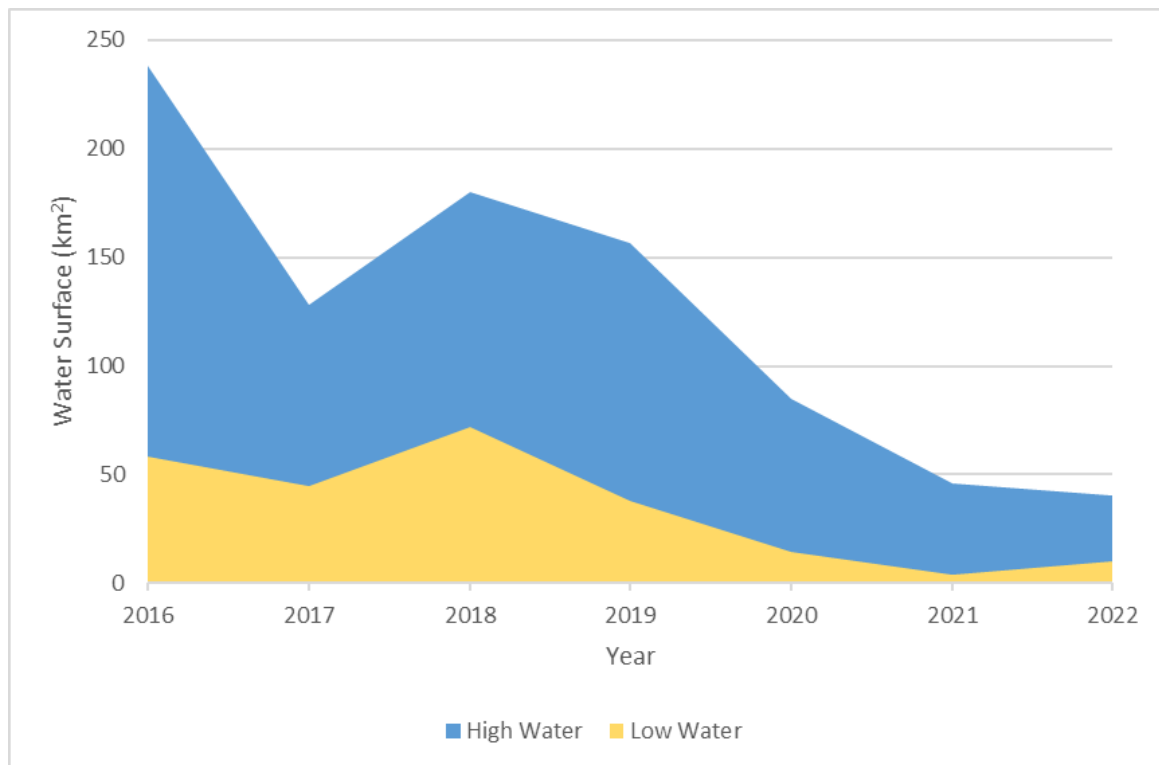
Figure 25 - Graph showing the water surface (km$^2$) for the target area through the year of 2016 up to 2022 in its high water stage (blue), and low water stage (yellow).

The data shows a dramatic decrease in water surface between 2016 and 2022 (Figure 25), roughly an 83% decrease from the high water of 2016 to the high water of 2022 was observed. With the exception of the year 2017, we see a steady decrease of water surface during high water up to 2019 and then a sharp decrease in 2020 that is preserved up to 2022. The different behavior of the year 2017 could be due to its early sensing date in January (Table 10).

The decrease in area between the high water and low water is on average 75%, and the water surface area during the low water stage has a similar behavior to the water surface area during the high water stage throughout the years (Figure 25). However, 2018 was exceptionally wet with a decrease of only 60% (Table 10), which could be due to the cloud cover in the data used, and 2021 was exceptionally dry with a decrease of 91% (Table 10).

## 5. SUMMARY

Remote sensing has already been proved to be a useful technique to monitor water bodies easily, cheaply and quickly. This work helps to broaden the horizon of possibilities of these techniques when applied to a complex and unique environment such as the Pantanal. Also, the workflow here presented assists the use of Sentinel-2 imagery to a broader range of objectives, since it has a better spatial, temporal and spectral resolution than the most commonly used sensors in water delineation.

Even though the subject of water surface extraction is widely discussed, it still has issues and it is still not suitable to all scenarios (Bijeesh- Narasimhamurthy, 2020). Therefore, this work helps to define a useful water extraction index method for the Pantanal region. The automated water extraction index for shadow areas (AWEIsh) coupled with the Otsu's algorithm thresholding proved to be a reliable method for water surface extraction, achieving a Kappa index of 0,87 (Table 7) and producing a 20 meters spatial resolution water surface extraction image (Figures 13, 14, 15, 16, 17, 18 and 19).

The analysis of the water surface changes between the seasons, however, highlighted that this method is not without shortcomings. The sampling of vegetation canopy during the dry season (figure 24) is an issue of this method that could be worked further. This, however, do not disable the method for delivering useful information as the accuracy evaluation demonstrated reliable results and overall a good Kappa index for all the images created (Table 9). With the proper treatment, the data acquired from this method can be used for water surface measurements and monitoring.

The application of this method to the target area unveiled a decrease in the water surface area of the region during the timespan of the study and mostly since 2020 (Figure 25). The water surface area during the high water ranged from 238 $km^2$ up to 40 $km^2$ (Table 10), while during the low water it ranged from 72 $km^2$ up to 4 $km^2$ (Table 10). On average, there was a 75% decrease in water surface area between the wet and dry season (Table 10).

This study, therefore, adds new data that corroborate to the worrying scenario of climatic change in the Brazilian Pantanal that is already being studied (Marengo et al., 2016; Lázaro et al., 2020). Most importantly, this work also provides a useful methodology that can be programmatically constructed to be automated and continuously generate water extraction maps for the region or be applied to a larger dataset without the need of human interference.

## 6. REFERENCES

Bazzo, J.C.-França De Freitas, D.A.-Leandro, M.-Silva, N.-Cardoso, E.L.-Santos, S.A. (2012):*Revista De Geografia (Ufpe) Aspectos Geofísicos E Ambientais Do Pantanal Da Nhecolândia. Geophysical and Environmental Aspects of the Pantanal Nhecolândia* 29.

Bhangale, U.-More, S.-Shaikh, T.-Patil, S.-More, N. (2020):*Analysis of Surface Water Resources Using Sentinel-2 Imagery*. Procedia Comput. Sci. 171, 2645–2654. https://doi.org/10.1016/j.procs.2020.04.287

Bijeesh, T. V.-Narasimhamurthy, K.N. (2020):*Surface water detection and delineation using remote sensing images: a review of methods and algorithms*. Sustain. Water Resour. Manag. 6. https://doi.org/10.1007/s40899-020-00425-4

Bishop-Taylor, R.-Sagar, S.-Lymburner, L.-Alam, I.-Sixsmith, J. (2019):*Sub-pixel waterline extraction: Characterising accuracy and sensitivity to indices and spectra*. Remote Sens. 11, 1–23. https://doi.org/10.3390/rs11242984

Bradski, G.-Kaehler, A. (2008):Learning OpenCV, Learning OpenCV.

Bukata, R.P.-Jerome, J.H.-Kondratyev, A.S.-Pozdnyakov, D. V (2018):Optical Properties and Remote Sensing of Inland and Coastal Waters. CRC Press.

Campbell, J.B.-Wynne, R.H. (2011):Introduction to remote sensing. Guilford Press.

Castilla - Castellano, G. (2003):*Object-oriented analysis of Remote Sensing images for land cover mapping: conceptual foundations and a segmentation method to derive a baseline partition for classification*. Dep. Econ. y Gestión las Explot. e Ind. For. Doctorado, 204.

Chuvieco, E. (2016):Fundamentals of satellite remote sensing: An environmental approach. CRC press.

Congalton, R.G. (1991):*A review of assessing the accuracy of classifications of remotely sensed data*. Remote Sens. Environ. 37, 35–46. https://doi.org/10.1016/0034-4257(91)90048-B

Congedo, L. (2021):*Semi-Automatic Classification Plugin: A Python tool for the download and processing of remote sensing images in QGIS*. J. Open Source Softw. 6, 3172. https://doi.org/10.21105/joss.03172

da Silva, C.J.-Silva, J.A.F. (1995):*No ritmo das águas do Pantanal*.

da Silva, J. dos S.V.-de Moura Abdon, M. (1998):*Delimitação do Pantanal brasileiro e suas sub-regiões*. Pesqui. agropecuária Bras. 33, 1703–1711.

Dong, P.-Chen, Q. (2017):LiDAR remote sensing and applications. CRC Press.

Feyisa, G.L.-Meilby, H.-Fensholt, R.-Proud, S.R. (2014):*Automated Water Extraction Index: A new technique for surface water mapping using Landsat imagery*. Remote Sens. Environ. 140, 23–35. https://doi.org/10.1016/j.rse.2013.08.029

Foody, G.M. (2002):*Status of land cover classification accuracy assessment*. Remote Sens. Environ. 80, 185–201.

Gatti, A.-Bertolini, A. (2013):*Sentinel-2 products specification document*. https//earth. esa. int/documents/247904/685211/Sentinel-2+ Prod. Specif. Doc. Acessed 13 April, 2023.

Gleick, P.H. (1993):Water in crisis. New York: Oxford University Press.

Grizonnet, M.-Michel, J.-Poughon, V.-Inglada, J.-Savinaud, M.-Cresson, R. (2017):*Orfeo ToolBox: Open source processing of remote sensing images*. Open Geospatial Data, Softw. Stand. 2, 1–8.

Guo, M.-Li, J.-Sheng, C.-Xu, J.-Wu, L. (2017):*A review of wetland remote sensing*. Sensors 17, 777.

Jiang, W.-Ni, Y.-Pang, Z.-Li, X.-Ju, H.-He, G.-Lv, J.-Yang, K.-Fu, J.-Qin, X. (2021):*An effective water body extraction method with new water index for sentinel-2 imagery*. Water 13, 1647.

Junk, W.J.-Piedade, M.T.F.-Lourival, R.-Wittmann, F.-Kandus, P.-Lacerda, L.D.-Bozelli, R.L.-Esteves, F. de A.-Nunes da Cunha, C.-Maltchik, L. (2014):*Brazilian wetlands: their definition, delineation, and classification for research, sustainable management, and protection*. Aquat. Conserv. Mar. Freshw. Ecosyst. 24, 5–22.

Landis, J.R.-Koch, G.G. (1977):*The measurement of observer agreement for categorical data*. Biometrics 159–174.

Lázaro, W.L.-Oliveira-Júnior, E.S.-Silva, C.J. da-Castrillon, S.K.I.-Muniz, C.C. (2020):*Climate change reflected in one of the largest wetlands in the world: an overview of the Northern Pantanal water regime*. Acta Limnol. Bras. 32.

Louis, J.-Debaecker, V.-Pflug, B.-Main-Knorn, M.-Bieniarz, J.-Mueller-Wilm, U.-Cadau, E.-

Gascon, F. (2016):*Sentinel-2 Sen2Cor: L2A processor for users*, in: Proceedings Living Planet Symposium 2016. Spacebooks Online, pp. 1–8.

Marengo, J.A.-Alves, L.M.-Torres, R.R. (2016):*Regional climate change scenarios in the Brazilian Pantanal watershed*. Clim. Res. 68, 201–213.

McFeeters, S.K. (1996):*The use of the Normalized Difference Water Index (NDWI) in the delineation of open water features*. Int. J. Remote Sens. 17, 1425–1432.

Otsu, N. (1979):*A threshold selection method from gray-level histograms*. IEEE Trans. Syst. Man. Cybern. 9, 62–66.

Phiri, D.-Simwanda, M.-Salekin, S.-Nyirenda, V.R.-Murayama, Y.-Ranagalage, M. (2020):*Sentinel-2 data for land cover/use mapping: A review*. Remote Sens. 12, 2291.

Pignatale, F. C. (2022): *Sen2Cor 2.11.00 Configuration and User Manual*.https://step.esa.int/thirdparties/sen2cor/2.11.0/docs/OMPC.TPZG.SUM.001%20 -%20i1r0%20-%20Sen2Cor%202.11.00%20Configuration%20and%20User%20Manual .pdf. Accessed 28 March 2023.

Reddy, G.P.O.-Singh, S.K. (2018):Geospatial technologies in land resources mapping, monitoring and management. Springer.

Sabins, F.F. (2007):Remote sensing: principles and applications. Waveland Press.

Sabins Jr, F.F.-Ellis, J.M. (2020):Remote sensing: Principles, interpretation, and applications. Waveland Press.

Shiklomanov, I.A. (1993):*World fresh water resources In: Gleick PH, editor. Water in crisis: a guide to the world's freshwater resources*.

Silio-Calzada, A.-Barquín, J.-Huszar, V.L.M.-Mazzeo, N.-Méndez, F.-Álvarez-Martínez, J.M. (2017):*Long-term dynamics of a floodplain shallow lake in the Pantanal wetland: Is it all about climate?* Sci. Total Environ. 605, 527–540.

USGS. (2018). What are the band designations for the Landsat satellites?https://www.usgs.gov/faqs/what-are-band-designations-landsat-satellites #publications. Accessed 12 April 2023.

Xie, H.-Luo, X.-Xu, X.-Pan, H.-Tong, X. (2016):*Automated subpixel surface water mapping from heterogeneous urban environments using Landsat 8 OLI imagery*. Remote Sens. 8,
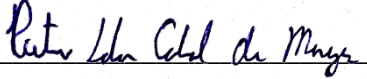
584.

Xu, H. (2006):*Modification of normalised difference water index (NDWI) to enhance open water features in remotely sensed imagery*. Int. J. Remote Sens. 27, 3025–3033.

Yang, X.-Chen, L. (2017):*Evaluation of automated urban surface water extraction from Sentinel-2A imagery using different water indices*. J. Appl. Remote Sens. 11, 26016.

Zhang, Y.-Gao, J.-Wang, J. (2007):*Detailed mapping of a salt farm from Landsat TM imagery using neural network and maximum likelihood classifiers: a comparison*. Int. J. Remote Sens. 28, 2077–2089.

# DECLARATION

I, undersigned *Pietro Laba Cabral de Menezes* (NEPTUN CODE: M6QWO1), declare that the present master's thesis is my original intellectual product in full and that I have not submitted any part or the whole of this work to any other institution. Permissions related to the use of copyrighted sources in this work are attached.

I AGREE to the publication of the accepted master's thesis in pdf form on the website of the Department of Cartography and Geoinformatics.

Budapest, *11, May, 2023*

*(signature of the student)*